INSTYTUT TECHNOLOGII MATERIAŁÓW ELEKTRONICZNYCH

MATERIAŁY ELEKTRONICZNE

ELECTRONIC MATERIALS

KWARTALNIK

T. 44 - 2016 nr 2

Wydanie publikacji dofinansowane jest przez
Ministerstwo Nauki i Szkolnictwa Wyższego

WARSZAWA ITME 2016

ADRES REDAKCJI
Instytut Technologii Materiałów Elektronicznych
ul. Wólczyńska 133, 01-919 Warszawa,
e-mail: ointe@itme.edu.pl;
www: matelektron.itme.edu.pl

KONTAKT
redaktor naczelny:
tel.: (22) 834 90 03 oraz (22) 639 58 05
sekretarz redakcji: (22) 639 55 29

PL ISSN 0209 - 0058
Kwartalnik notowany na liście czasopism naukowych Ministerstwa Nauki i Szkolnictwa Wyższego
7 pkt. - wg komunikatu MNiSW.

Opublikowane artykuły są indeksowane w bazach danych: BazTech, CAS - Chemical Abstracts oraz Index Copernicus

Publikowane artykuły mające charakter naukowy są recenzowane przez samodzielnych pracowników naukowych.

Wersja papierowa jest wersją pierwotną.
Kwartalnik publikowany jest w otwartym dostępie.
Nakład: 200 egz.

Na okładce: ceramika Y_2O_3
Autor zdjęcia: dr inż. Anna Piątkowska
Projekt: „*Właściwości mechaniczne i odporność na szoki termiczne przezroczystej ceramiki Y_2O_3 w funkcji mikrostruktury i temperatury”,* finansowany przez Narodowe Centrum Nauki.
Koordynator projektu: dr Marek Boniecki

SPIS TREŚCI - CONTENTS

STRESZCZENIA ARTYKUŁÓW

ME 44 - 2 - 2016

Właściwości elektryczne materiałów stykowych Ag-C i Cu-C

ME 44, 2, 2016, s. 4

Przemysłowe otrzymywanie rozmaitych form węgla – grafenu, nanorurek, fulerenów – rozszerzyło gamę materiałów kompozytowych, w których stanowią one fazę wzmacniającą matryc metalicznych. Oczekiwano, że grafenowa faza wzmacniająca polepszy cechy elektryczne, cieplne i wytrzymałościowe takich kompozytów. Szczególnie obiecującymi są kompozyty z matrycami Cu lub Ag znajdujące zastosowania w mikroelektronice i optoelektronice, przemysłach lotniczym i samochodowym. Specyficzna grupa tych kompozytów stosowana jest w rozmaitych elementach układów elektrycznych jako wyłączniki etc. Do grupy tej należą między innymi kompozyty Ag-W; Ag-WC, Ag-WC-C lub Cu-W. Prezentowane wyniki badań elektrycznych kompozytów Cu(Ag)/GF poszerzają zbiór właściwości materiałów stosowanych w powietrznych i próżniowych stykach elektrycznych.

Skaningowy mikroskop elektronowy pracujący w zakresie niskich wartości napięcia przyspieszającego jako unikatowe narzędzie do charakteryzacji warstw grafenu

ME 44, 2, 2016, s. 11

Próbki grafenu otrzymywanego metodą chemicznego osadzania z fazy gazowej na podłożach Cu poddano badaniom przy użyciu komercyjnego skaningowego mikroskopu elektronowego (SEM) pracującego w zakresie niskich wartości napięcia przyspieszającego. Optymalizacja warunków obrazowania SEM prowadzona w trybie dwukanałowym (rejestracja obrazów SE1 i BSE podczas tego samego skanu) pozwoliła na wizualizację typowych cech grafenu na Cu takich jak fałdy, pęknięcia i dodatkowe warstwy. Mechanizm kontrastu związanego ze zmianami liczby warstw grafenu obserwowanego w obrazach BSE został przedstawiony w oparciu o detekcję elektronów BSE o niskich stratach energii. Przeciwutleniające właściwości grafenu na metalicznych podłożach zostały potwierdzone poprzez możliwość obserwacji kontrastu kanałowania elektronów w podłożach Cu przy energii elektronów pierwotnych rzędu 0,5 keV.

Stabilność wysokotemperaturowa ekologicznych rezystorów grubowarstwowych

ME 44, 2, 2016, s. 17

W związku z Dyrektywą RoHS, która weszła w życie w 2006 roku producenci materiałów elektronicznych zostali zmuszeni do wyeliminowania m.in. ołowiu i jego związków ze składów tych materiałów. Dyrektywa wymusiła zmianę składu past służących do wytwarzania rezystorów grubowarstwowych szeroko rozpowszechnionych w konsumenckim sprzęcie elektronicznym. Autorzy zaproponowali nowatorskie pasty rezystywne zdolne w pełni zastąpić pasty oparte o ołów i jego związki. Ponadto zostały przeprowadzone badania odporności na narażenia termiczno-prądowe, które ujawniły przewagę użytkową w aspektach stabilności rezystancji na cykliczne narażenia temperaturowe nowych past wobec past tradycyjnych.

THE ARTICLES ABSTRACTS

ME 44 - 2 - 2016

Electrical properties of Ag-C and Cu-C contact materials

ME 44, 2, 2016, p. 4

Industrial production of various forms of carbon, including graphene, nanotubes, and fullerenes, expanded the range of composite materials for which they constitute the reinforcing phase of metallic matrices. It was expected that the graphene form (GF) reinforcing phase would improve the electrical, thermal, and mechanical properties of such composites. Composites with Cu and Ag matrices, having a wide range of applications in micro- and optoelectronics, aerospace and automotive industries, proved to be particularly promising. A specific group of these composites is used in a variety of electrical circuits for electrical switches, contactors, circuit breakers, voltage regulators, and arcing tips. Among others, this group includes composites such as Ag-W, Ag-WC, Ag-WC-C, or Cu-W. The presented results of electrical tests performed for the Cu (Ag) /GF composites extend the number of properties of materials used in air and vacuum electrical contacts.

Scanning electron microscope at low voltage operation – a unique characterization tool for graphene layers

ME 44, 2, 2016, p. 11

Graphene grown on Cu foils by chemical vapor deposition (CVD) technique has been investigated using commercially available scanning electron microscope at low voltage operation. The optimized conditions of SEM imaging carried out in a double-channel mode (registering secondary electrons type 1 (SE1) and backscattered electrons (BSE) images in a single scan) allowed for the visualization of typical features of graphene on Cu, such as folds, cracks and add-layers. The mechanism of thickness contrast observed in the BSE images was described in terms of low loss-BSE detection. Antioxidant qualities of graphene sheets on metallic substrate were confirmed by the ability of observation of the channeling contrast in Cu substrates at primary electrons energy of 0.5 keV.

High temperature stability of eco-friendly thick-film resistors

ME 44, 2, 2016, p. 17

Under the EU directive on the Restriction of Hazardous Substances (RoHS) implemented in 2006, producers of electronics materials were obliged to eliminate lead and its compounds from the compsition of their products. As a consequence of this directive the changes affected the compositions of pastes used in the production of thick-film resistors, widely used in mass electronics. The authors have developed new compositions for the resistive thick film pastes, to replace the ones based on lead. Moreover, the thermal and electrical studies showed the advantage of the new compositions over the traditional ones in terms of resistance stability under temperature cyclic test.

Electrical properties of Ag-C and Cu-C contact materials

Katarzyna Pietrzak[1], Andrzej Gładki[1], Krystyna Frydman[1], Danuta Wójcik-Grzybek[1], Kamil Kaszyca[1], Piotr Borkowski[2]

[1] Institute of Electronic Materials Technology
133 Wólczynska Str., 01-919 Warsaw, Poland
e-mail: Katarzyna.Pietrzak@itme.edu.pl

[2] Department of Electrical Apparatus,
Lodz University of Technology
B. Stefanowskiego 18/22, 90-924 Lodz, Poland

Abstract: Industrial production of various forms of carbon, including graphene, nanotubes, and fullerenes, expanded the range of composite materials for which they constitute the reinforcing phase of metallic matrices. It was expected that the graphene form (GF) reinforcing phase would improve the electrical, thermal, and mechanical properties of such composites. Composites with Cu and Ag matrices, having a wide range of applications in micro- and optoelectronics, aerospace and automotive industries, proved to be particularly promising. A specific group of these composites is used in a variety of electrical circuits for electrical switches, contactors, circuit breakers, voltage regulators, and arcing tips. Among others, this group includes composites such as Ag-W, Ag-WC, Ag-WC-C, or Cu-W. The presented results of electrical tests performed for the Cu (Ag) /GF composites extend the number of properties of materials used in air and vacuum electrical contacts.

Key words: contact materials, composite materials, graphene form

Właściwości elektryczne materiałów stykowych Ag-C i Cu-C

Streszczenie: Przemysłowe otrzymywanie rozmaitych form węgla – grafenu, nanorurek, fulerenów – rozszerzyło gamę materiałów kompozytowych, w których stanowią one fazę wzmacniającą matryc metalicznych. Oczekiwano, że grafenowa faza wzmacniająca polepszy cechy elektryczne, cieplne i wytrzymałościowe takich kompozytów. Szczególnie obiecującymi są kompozyty z matrycami Cu lub Ag znajdujące zastosowania w mikroelektronice i optoelektronice, przemysłach lotniczym i samochodowym. Specyficzna grupa tych kompozytów stosowana jest w rozmaitych elementach układów elektrycznych jako wyłączniki etc. Do grupy tej należą między innymi kompozyty Ag-W; Ag-WC, Ag-WC-C lub Cu-W. Prezentowane wyniki badań elektrycznych kompozytów Cu(Ag)/GF poszerzają zbiór właściwości materiałów stosowanych w powietrznych i próżniowych stykach elektrycznych.

Słowa kluczowe: materiały stykowe, materiały kompozytowe, formy grafenowe

1. Introduction

Composite materials with Cu and Ag matrices are used as electrical contacts in a number of applications such as electrical switches, residual current circuit breakers, contactors, automatic circuit breakers, voltage regulators, relays and current dividers, as well as blade electrodes. Depending on the target application, the incorporation of reinforcing phases of contact materials can be different, e.g. W[1], WC [2], Ni [3], SnO_2 [4], and C [5 - 6]. Until now, carbon forms used in contact composite materials included diverse allotropic carbon structures [7 - 8], e.g. graphite in the form of fibers, grains, and flakes [9]. Materials found in electrical contacts require both coexistence and complementarity of qualities such as good thermal conductivity, resistance to wear and deformation, erosion and welding resistance, as well as low and stable electrical resistance. Ag-C composites with the carbon content of around (3 ÷ 5)% wt. are used in air-connectors. They are characterized by high resistance to welding, as well as low contact and corrosion resistance in the air environment. Cu-C (3 ÷ 5)% wt. composite materials are used in welding-resistant contacts for currents in the 30 - 100 kA range. The relatively low hardness and strength of these materials make them easy to separate when serving as contacts. They also oxidize copper easily and, in consequence, are most frequently used either in vacuum or oily electrical systems. Experimental work on graphene (G) [10 - 11] and its geometrical forms (GF), i.e. nanotubes (CNT) [12] and graphene powder (GP) [13], and Cu(Ag)/CNT(GP) composite materials [14 - 15], as well as a strong commercial market of graphene materials, make it possible to carry out research work focused on the application of Ag--GF and Cu-GF contacts. There are several reasons, why the introduction of carbon based nanofillers (nanofibers, nanotubes) into metallic matrices is a difficult task [16]. The results presented in this paper are closely related to the research into arc erosion and electrical resistance of the Cu-3% v CNT(GP) and Ag-3% v CNT(GP) contacts. The volume share of 3% v CNT(GF) was derived from the correlation between thermal conductivity and hardness of the tested composite materials. More extensively, the problems regarding the preparation and properties of composites reinforced with nanostuctures are shown in [8].

This sequence of the procedures for preparing the composites, helped to obtain materials with high density, hardness and thermal conductivity. The features that are important for contact materials.

2. Experimental procedure

2.1. Materials

The granulometric characteristics of the starting materials are shown in Tab. 1, whereas Fig. 1 presents the Raman spectra of both graphene forms used before sonication process. Results coming from Renishaw inVia Confocal Raman Microscope with laser ND:YAG of 532 nm line.

The analysis of the spectra proved MWNTs to be a material variation of reduced graphene oxide, while GP is a collection of objects consisting of several individual flakes of defected graphene. Both forms of graphene used in the study were dry forms of carbon. Multi-walled carbon nanotubes (MWNTs) appeared as heavily entangled balls with diameters larger than 30 microns. Graphene nanopowder showed up in the form of aggregated clusters of more than 5 microns in diameter. It can be assumed from the analyses that the planes of carbon are strongly defected, as evidenced by the high intensity of modules D and D '. Activation mode D" is related to the concentration of sp3 hybridized atoms and is proportional to the number of defects in the planes of carbon. 2D a single band, extended (compared to the SLG) indicates the material thickness of layers 4 - 6 different than the Bernal arrangement (ABAB, as in graphite). Intensity ratio I2D / IG is in the range 0.4 - 0.6. Intensity ratio ID / IG is in the range 0.4 - 0.8. The distance between the defects ranges from 50 to 25 nm, with a substantial edge defects (mod D '). Shift modes at positions G and 2D indicate the stress occurring in the sample.

On average, the thermal conductivity of an aggregated or entangled graphene material is two orders lower than for pure graphene – ~ 5500 $W(mK)^{-1}$. Its electrical conductivity is reduced to a lesser, but equally important extent when compared to pure graphene – ~ 10^7 Sm^{-1}. To produce a composite contact material, it was therefore necessery to adopt procedures entailing detangling and separation of carbon forms. These procedures consisted in breaking up large concentrations of carbon forms in the sound field. The pulse sound field working in the 1 sec/1 sec ON/OFF mode for 4 minutes exerted influence on MWNTs in the aqueous micellar solution of Triton X-100 as well as GP in pure isopropyl alcohol. The solutions were then centrifuged at 5000 rpm, at intervals from 10 to 20 minutes. The concentrations of the solutions after centrifugation were determined spectrophotometrically by comparing the transmission of light for the known GF masses to the transmission for respective solutions after centrifugation. MWNTs solutions were filtered through a layer of Cu or Ag powders, and washed several times with deionized

Tab. 1. Details of raw materials.
Tab. 1. Charakterystyka materiałów wyjściowych.

Materials		Producer	Geometric characteristics of materials (data of producers)
Ag	Ag (1000)	Innovator	10 μm
Cu	Cu	Aldrich	10 μm
C	Multiwalls nanotubes (MWNTs)	Aldrich	Φ 110 - 170 nm, length 5 - 9 μm
	Graphene nanopowder (GP)	Skayspring Nanomaterials Inc.	1 - 5 nm Surface area 750 m^2/g

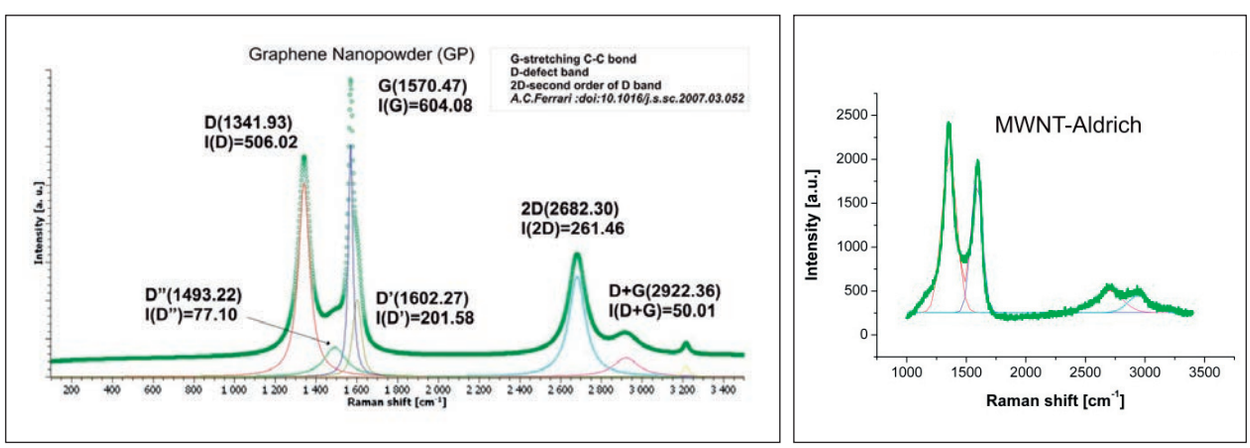

Fig. 1. Raman spectrum of graphene materials.
Rys. 1. Ramanowskie widma materiałów grafenowych.

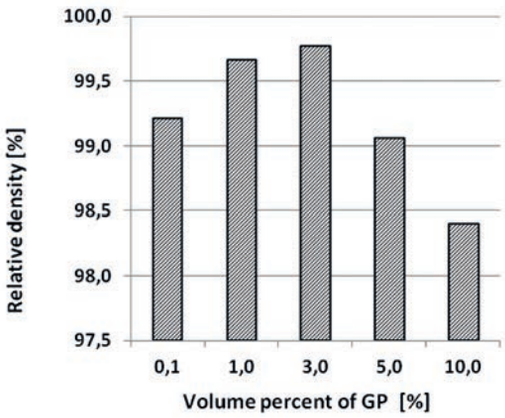

Fig. 2. Density of Cu-GP composites with different GP content.
Rys. 2. Gęstość kompozytów Cu-GP o różnej zawartości GP.

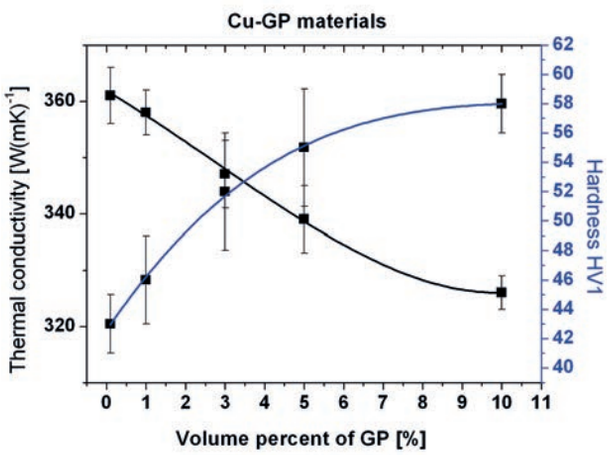

Fig. 3. Correlation of thermal conductivity and hardness for composites with different content of GP.
Rys. 3. Korelacje pomiędzy przewodnictwem cieplnym i twardością kompozytów o różnej zawartości GP.

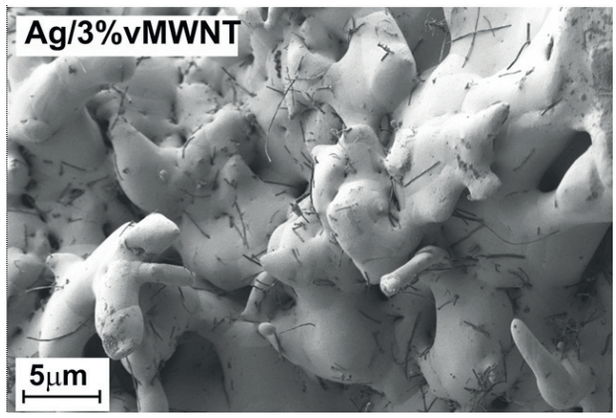

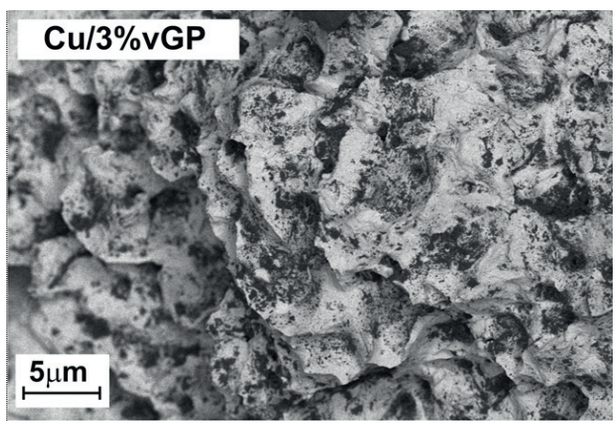

Fig. 4. SEM images of the composite fractures of Ag/3%v MWNTs and Cu/3% v GP.
Rys. 4. Obrazy SEM przełomów kompozytów Ag/3%v MWNTs and Cu/3% v GP.

water. GP solutions in ethanol were mixed with the powder and evaporated. The resultant composite powders with Ag and Cu matrices, in the (0.1 ÷ 10)% v GP and (0.1 ÷ 5)% v MWNTs range, were sintered by the Spark Plasma Sintering (SPS) method. The sintering conditions were as follows: pressure 50 MPa; time 15 min; vacuum 10^{-5} hPa, and temperatures Ag/GF-850°C; Cu/GF-950°C. The density of composite materials reached 99% of the theoretical density (Fig. 2). Thermal conductivity and hardness were measured for the obtained composites. Fig. 3 shows the interrelationship between the thermal conductivity of the Cu-GP composite and its hardness as a function of the percentage share of the graphene form.

The analysis of the graph shows that for this particular relationship the optimum conditions are offered by the Cu3.5% v GP composite. The results of similar analyses performed for the Cu MWNTs and Ag-GP(MWNTs) turned out to be a set of values in the (2.7 ÷ 4.3)% v GP (MWNTs) range for both Cu or Ag matrices. Therefore, electrical contacts were tested using Cu and Ag composites containing 3% of the volumetric reinforcing phases of the GP and MWNTs. The representative images showing the structures of Ag/3% v MWNTs and Cu/3% v GP composite can be found in Fig. 4. Embedded in the matrix the nanometric carbon structures were invisible on metallographic cross section but could be seen on composite fractures. It should be noted that there is good adhesion and uniform distribution of MWNTs in the silver matrix. A similar character was observed for graphene nanopowder. In the copper matrix flake clusters can be observed, decorating the grain boundaries of copper. Also, the nanotubes in the copper matrix form bunches with distinctive pores on the copper-MWNT interfaces.

2.1. Electrical test

Plates in the form of cylinders having a diameter of 8 mm and a height of 1 mm, sintered by SPS, were used for the electrical tests. Research into arc erosion and contact resistance was carried out using the original computer test system, designed and built in the Department of Electrical Apparatus of the Lodz University of Technology [7, 16]. The current path of the tester is equipped with two contact handles. A single, 3-second cycle of the experiment consists in switching the contact tips on and off. The device has 10 identical yet independent current paths.

Tab. 2. Mechanical and electrical parameters of testing device.
Tab. 2. Mechaniczne i elektryczne parametry testera.

Mechanical parameters	Unit	Value
Contact diameter	mm	8
Contact gap	mm	5
Contact tilt	mm	2
Contact tip pressure force	N	10
Opening spring force	N	30
Electrical parameters	**Unit**	**Value**
Test voltage	V, Hz	230, 50
Test current (peak value)	A (AC)	60
Circuit power coefficient	-	1
Operating frequency	cycles/h	1200

The whole system is controlled with copyright software in the automatic mode. The testing device is based on a computer system for measurement data (current, voltage) acquisition. Basic parameters of mechanical and electrical tests are provided in Tab. 2.

The parameter determining the level of arc erosion is the weight loss of the contacts. In general, the energy of an electric arc and mechanical opening cause detachment of the material from the surface of the contacts. The loss of weight as a function of the number of cycles is a measure of the electrical and mechanical resistance of the contact to the electric arc. The measurement of contact resistance indicates changes in the subsurface layer of the contact material, affecting the contact resistance. The voltage drop over the electrical contact as well as its resistance have an influence on the circuit operation, and consequently on the temperature and the safety of electrical devices that operate in this circuit. Contact resistance was measured experimentally based on the voltage drop across a pair of closed contacts and the flow of the 5 A electric current amperage. This measurement was carried out as a function of the number of cycles.

3. Results

In total, the number of the performed switching cycles for the Ag-matrix composite was $N = 10^5$. For Cu-matrix composites the number of $N = 10^4$ cycles was the upper limit from the point of view of arc erosion resistance. The representative images of tip surfaces after the end of the test with the maximum number of cycles are presented in Fig. 5. Differences in tip surface morphology are clearly seen in Fig. 5a. The contact surface of the Ag3% v GP composite has numerous small craters and is significantly developed. The tip based on the Ag3% v MWNTs composite has a much less developed surface, with many ovoid hills on top. The morphology of the Cu-tip surfaces is very much alike. Numerous craters and areas with oxidized layers are observable in Fig. 5b.

The edges are decorated by the drops of the composite material. In all SEM images of the contact surface, presented in Fig. 6, the influence of the arc's high temperature is visible. The drops of molten composite material appear on the surfaces of silver tips, whereas granules with extended surfaces are observed for the Cu tip. Additionally, cracks on the surfaces of both types of GP-reinforced matrices are clearly visible. The surface cracks are imperceptible for MWNT-reinforced composites. The analysis of SEM images showing the tips' microsection in Fig. 7 indicates differences in the composite structures with nanotubes and nanopowders. The highly loosened centers of zone overheating are formed for GP-reinforced Ag-matrix composites. They are seen as pores, from which the composite material is poured. Gray overheating channels, with a subtle nanocrystalline structure, are visible for the Ag/3% v MWNT composites. The edge zone of the tips forms a solid, but very fine-grained structure. In the case of the Cu3% v GP composite, vast gray centers of copper oxide mixtures can be observed in the superficial zone. For the Cu matrix reinforced with nanotubes, the width

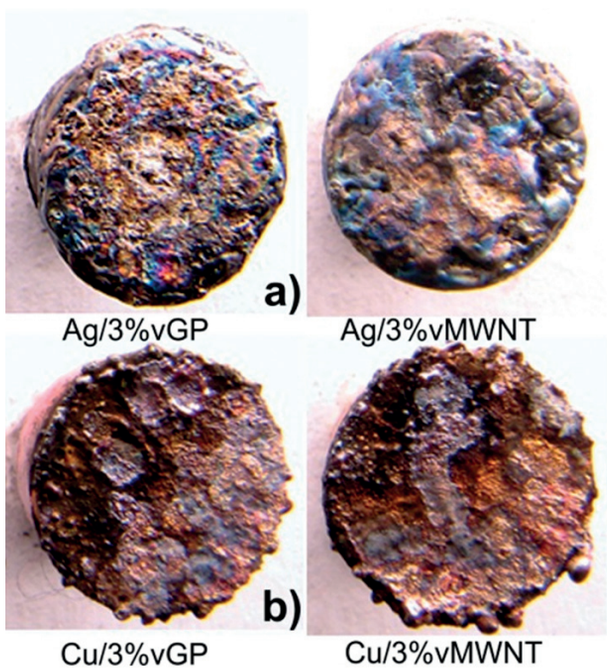

Fig. 5. The surface images of contact tips after the end of tests; a) with Ag matrices, b) with Cu matrices.
Rys. 5. Obrazy powierzchni nakładek stykowych po zakończeniu testu: a) z osnową Ag, b) z osnową Cu.

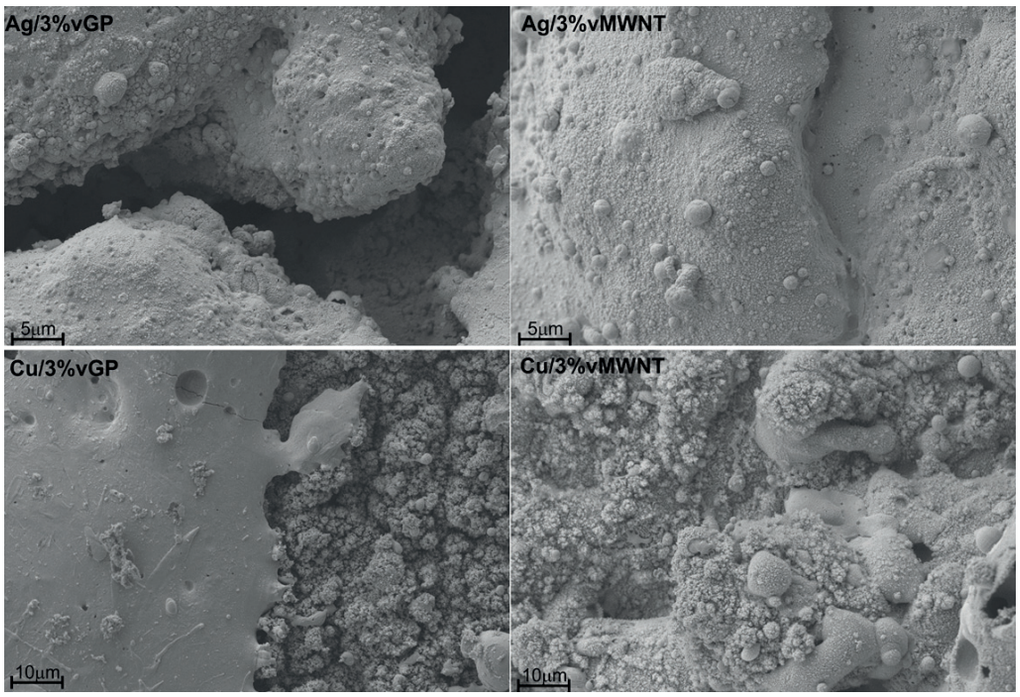

Fig. 6. The SEM images of contact tips surfaces after the end of tests.
Rys. 6. Obrazy SEM powierzchni nakładek stykowych po zakończeniu testu.

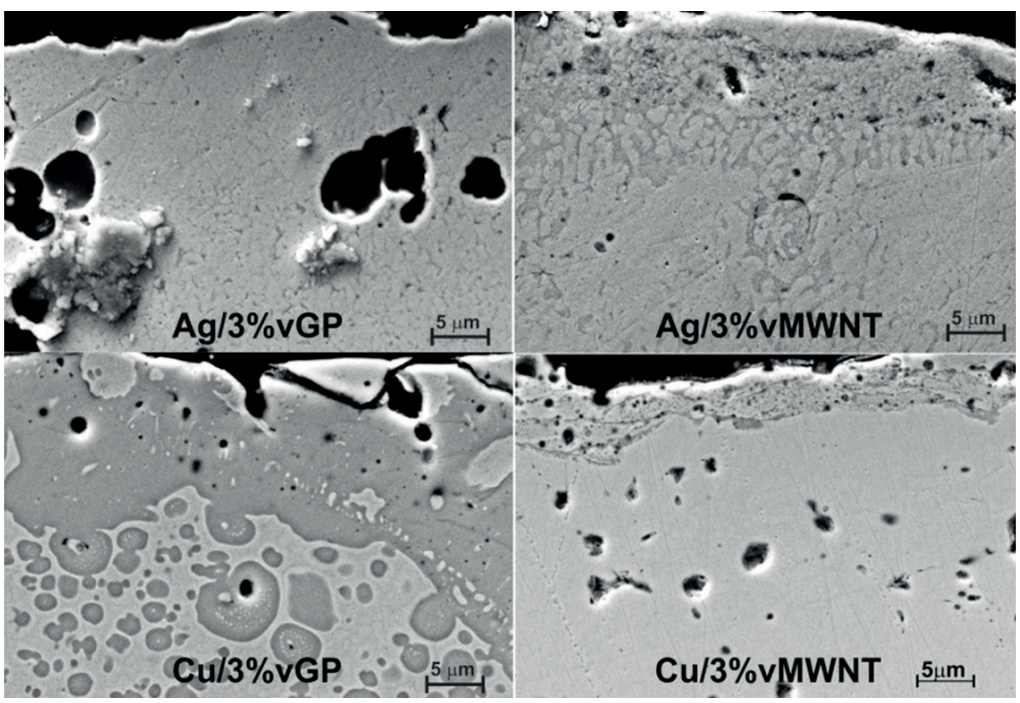

Fig. 7. SEM images of the metallographic sections of contact tips with different matrices and reinforcement phases.
Rys. 7. Obrazy SEM zgładów nakładek stykowych o różnych osnowach i fazach wzmacniających.

of the oxidized layer is many times smaller and quite well separated from the core tip.

The measurement results of the weight loss of the contact tips and their contact resistance are shown in Fig. 8.

The left-hand axes on the charts in Fig. 8 indicate the mass losses of the tips, while the right-hand Y-axes show contact resistance. It should be noted that contact resistance for both types of matrices is not dependent on the used reinforcing phase. Moreover, the absolute values of contact resistance for two kinds of materials differ significantly. For Ag matrices, resistance after N = 100 k operating cycles amounts to ~ 150 μΩ as presented in Fig. 8a. On the other hand, Fig. 8b shows that for Cu matrices it reaches 400 μΩ only after 20 k cycles. Depending on the

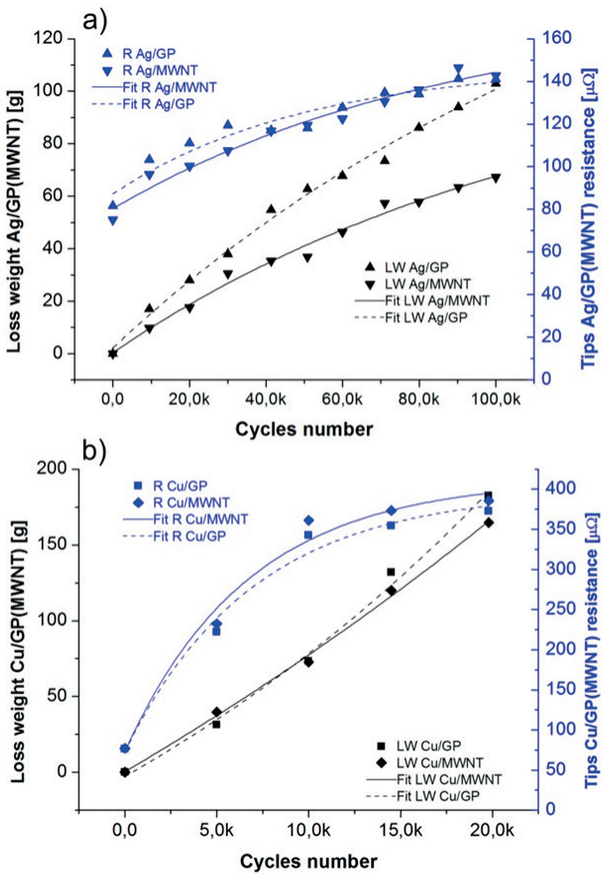

Fig. 8. The loss of mass and electrical resistance of contact materials vs. number of switching cycles: a) Ag/3% v GP(MWNTs), b) Cu/3% v GP(MWNTs) materials.
Rys. 8. Ubytek masy i opór elektryczny materiałów stykowych w funkcji liczby cykli łączeniowych: a) Ag/3% v GP(MWNTs), b) Cu/3% v GP(MWNTs) materials.

type of the reinforcing phase, mass losses are significant in contacts with the silver matrix. The loss of weight for silver contacts with nanotubes is two times lower than for those reinforced with GP (see Fig. 8a). The weight loss percentage for Cu/3%v GP composite (MWNTs) contacts is about 40%., for Ag/3% v MWNTs contacts it reaches the level of 10% of the starting material, and for the Ag/3% v GP composite it equals 20%.

4. Summary and conclusions

Correlation studies of thermal conductivity and hardness demonstrated that the optimal volume fraction of graphene forms for composite contact materials is around 3%. The performed electrical tests showed that:

- Surfaces of contacts made of cupreous composites are rapidly oxidized when exposed to electrical arc in atmospheric air. The addition of graphene forms does not protect the contact material against this type of corrosion. No protective effect can be observed when using graphene forms, unlike in the case of composites coated with graphene or exposed only to the slow action of air.
- After the arc action, contact materials based on silver revealed the existence of clear structural differences between composites with the GP and MWNTs. The Ag/3% v MWNTs composite turned out to be tougher in operation, with its weight loss being two times lower than for Ag/3% v GP contacts. In contrast, the electrical resistance of both composites was comparable in the whole range of cycles.

Acknowledgment

The results presented in this paper were obtained as part of the "GRAMCOM" project (Contract No Graftech/NCBiR/10/29/2013 with the National Centre for Research and Development) within the framework of the GRAF--TECH program.

References

[1] Bukhanovsky V. V., Grechanyuk N. I., Minakova R. V., Mamuzich I., Kharchenko V. V., Rudnitsky N. P.: Production technology, structure and properties of Cu–W layered composite condensed materials for electrical contacts. *International Journal of Refractory Metals and Hard Materials*, 2011, 29, 5, 573 – 58

[2] Findik F., Uzun H.: Microstructure, hardnes and electrical properties of silver - based refractory contact materials, *Materials & Design*, 2003, 24, 489 – 492

[3] Wu C., Weng D. Yi, W., Li S., Zhou J., Zheng F.: Arc erosion behavior of Ag/Ni electrical contact materials, *Materials & Design,* 2015, 85, 511 – 519

[4] Xu W., Canfield N. L., Wang D., Xiao J., Nie Z., Zhang J. - G.: A three-dimensional macroporous Cu/SnO_2 composite anode sheet prepared via a novel method, *Journal of Power Sources*, 2010, 195, 21, 7403 – 7408

[5] Kaczmar J. W., Pietrzak K., Włosiński W.: The production and application of metal matrix composite materials, *Journal of Materials Processing Technology*, 2000, 106, 1 – 3, 58 – 67

[6] Berner A., Mundim K .C., Ellis D. E., Dorfman S., Fuks D., Evenhaim R.: Microstructure of Cu–C interface in Cu-based metal matrix composite, *Sensors and Actuators A: Physical*, 1999, 74, 1 – 3, 86 – 90

[7] Borkowski P., Walczuk E., Wójcik-Grzybek D., Frydman K.: Electrical properties of Ag-C contact materials containing different allotropes of carbon, 25th International Conference on Electrical Contacts and 56th IEEE Holm Conference on Electrical Contacts, 2010, Charleston, 167 - 175

[8] Pietrzak K., Sobczak N., Chmielewski M., Homa M., Gazda A., Zybala R., Strojny-Nedza A.: Effect of carbon allotropic forms on microstructure and thermal properties of Cu-C composites produced by SPS, *Journal of Materials Engineering and Performance*, 2016, 25(8), 3077 - 3083

[9] Kováčik J., Bielek J.: Electrical conductivity of Cu/graphite composite material as a function of structural characteristics, *Scripta Materialia*, 1996, 35(2), 239 - 246

[10] Novoselov K. S., Geim A. K., Morozov S. V., Jiang D.: Two-dimensional gas of massless Dirac Fermions in graphene, *Nature*, 2005, 438 (7065), 197 - 200

[11] Bonaccorso F., Lombardo A., Tawfique H., Zhipei S., Colombo L., Ferrari A. C.: Production and processing of graphene and 2d crystals, *Materials Today*, 2012, 15(12), 564 - 589

[12] Lehman J. H., Terrones M., Mansfield E. et al.: Evaluating the characteristics of multiwall carbon nanotubes, *Carbon*, 2011, 49, 2581 – 2602

[13] Pop E. V., Varshney A., Roy K.: Thermal properties of graphene, *Fundamentals and Applications MRS Bull*, 2012, 37, 1273

[14] Wejrzanowski T., Grybczuk M., Chmielewski M., Pietrzak K., Kurzydlowski K. J., Strojny-Nedza A.: Thermal conductivity of metal-graphene composites, *Materials and Design*, 2016, 99, 163 – 173

[15] Chen F., Ying J., Wang Y. et al.: Effect of graphene content on the microstructure and properties of copper matrix composites, *Carbon*, 2016, 96, 836 - 842

[16] Neubauer E. , Kitzmantel M., Hulman M., Angerer P.: Potential and challenges of metal-matrix-composites reinforced with carbon nanofibers and carbon nanotubes, *Composite Science and Technology*, 2010, 70, 2228 - 2236

Scanning electron microscope at low voltage operation – a unique characterization tool for graphene layers

Iwona Jóźwik
Instytut Technologii Materiałów Elektronicznych
ul. Wólczyńska 133, 01 - 919 Warszawa
e-mail: Iwona.Jozwik@itme.edu.pl

Abstract: Graphene grown on Cu foils by chemical vapor deposition (CVD) technique has been investigated using commercially available scanning electron microscope at low voltage operation. The optimized conditions of SEM imaging carried out in a double-channel mode (registering secondary electrons type 1 (SE1) and backscattered electrons (BSE) images in a single scan) allowed for the visualization of typical features of graphene on Cu, such as folds, cracks and add-layers. The mechanism of thickness contrast observed in the BSE images was described in terms of low loss-BSE detection. Antioxidant qualities of graphene sheets on metallic substrate were confirmed by the ability of observation of the channeling contrast in Cu substrates at primary electrons energy of 0.5 keV.

Key words: graphene, graphene characterization, low-kV scanning electron microscopy

Skaningowy mikroskop elektronowy pracujący w zakresie niskich wartości napięcia przyspieszającego jako unikatowe narzędzie do charakteryzacji warstw grafenu

Streszczenie: Próbki grafenu otrzymywanego metodą chemicznego osadzania z fazy gazowej na podłożach Cu poddano badaniom przy użyciu komercyjnego skaningowego mikroskopu elektronowego (SEM) pracującego w zakresie niskich wartości napięcia przyspieszającego. Optymalizacja warunków obrazowania SEM prowadzona w trybie dwukanałowym (rejestracja obrazów SE1 i BSE podczas tego samego skanu) pozwoliła na wizualizację typowych cech grafenu na Cu takich jak fałdy, pęknięcia i dodatkowe warstwy. Mechanizm kontrastu związanego ze zmianami liczby warstw grafenu obserwowanego w obrazach BSE został przedstawiony w oparciu o detekcję elektronów BSE o niskich stratach energii. Przeciwutleniające właściwości grafenu na metalicznych podłożach zostały potwierdzone poprzez możliwość obserwacji kontrastu kanałowania elektronów w podłożach Cu przy energii elektronów pierwotnych rzędu 0,5 keV.

Słowa kluczowe: grafen, charakteryzacja grafenu, niskoenergetyczna skaningowa mikroskopia elektronowa

1. Introduction

Graphene on a copper substrate has attracted broad attention of researchers and industrialists all over the world, mostly due to its high quality and the possibility of achieving a monolayer graphene film which can be efficiently transferred and easily implemented in mass production [1 - 2]. Various unique properties of graphene have created high expectations for a number of applications in emerging technologies [3 - 4]. Nevertheless, graphene layers are atomically thick, and the overall electronic properties of a sample are determined by the number of layers present. Therefore, it is of great importance to be able to experimentally determine the number of graphene layers in a sample, particularly for device fabrication. Characterization of graphene films is essential for the quality control purposes. Common techniques include optical microscopy [5 - 7], atomic force microscopy [8 - 9], Raman spectroscopy, transmission electron microscopy [12 - 14], Auger electron spectroscopy [15], etc. Scanning electron microscopy (SEM) is getting more popular for imaging graphene because it is a rapid, non-invasive and effective imaging technique which is complementary to most other techniques. Particularly, many electronic applications require uniform and defect free graphene in large area. SEM has the advantages in detecting impurities, ruptures, folds, voids and discontinuities of synthesized or transferred graphene on a variety of substrates. However, SEM imaging of graphene is challenging, mainly due to the fact that the ultra-thin graphene film is *transparent* to sufficiently high energy of electron beam. Hence SEM images easily display the morphologies of the substrate beneath the graphene, not the graphene itself. Low beam energy is required to image graphene and an efficient, high performance electron detector is required for detecting low energy electrons which provide the best contrast and topographic sensitivity. Imaging graphene with a low beam voltage field emission scanning electron microscope (LV FE-SEM) is very promising because of its unique combination of high resolution, a small beam/specimen interaction volume, enhanced contrasts and the capability of revealing more surface details [16 - 20].

2. Experimental procedure

Graphene single- (SL) and multilayers (ML) grown by chemical vapor deposition (CVD) method on polycrystalline Cu substrates were subjected to SEM investigation

with low energy (less than 1 keV) electrons using Auriga CrossBeam Workstation (Carl Zeiss) equipped with the In-lens SE (true SE1) detector and Energy selective Backscattered electrons (EsB, low-loss BSE) detector, both positioned on the optical axis of the Gemini® column. In front of the entry system on the axis of the BSE detector there is an energy filtering grid integrated into the electron optical detection system, that can be adjusted in its retarding potential from 0 to 1500 volts. This grid allows only BSEs with energies greater than the grid energy to be detected. The energy of the primary electrons was adjusted to effectively reveal all the features of the studied samples in terms of graphene characterization. The presence of graphene has been independently confirmed by Raman spectroscopy measurements.

3. Results and discussion

The contrast in the images of SE1 detector (especially at low kV operation) is usually driven by the differences in the topography of the sample, thanks to the angular distribution of these electrons, as well as the small interaction volume [21]. However, other factors, such as sample surface potential, work function or crystallinity may strongly influence the contrast mechanisms as well. In most cases, it is rather unusual that only one factor will take control over the mechanism of contrast generation, so one should keep in mind that the origin of the observed contrast may by the result of phenomena superposition.

The design of the semi-in-lens detector of backscattered electrons applied in the system used, assures the imaging with low-loss BSE (LL-BSE), i.e. these electrons which were scattered in the single events almost elastically at high angles. Typically, the contrast in the images of LL-BSE is sensitive even to slight changes in the composition of the analyzed samples. However, when applied to imaging at low primary energies, it allows for visualization of the information from the few very first atomic layers of the sample. In case of thin films, the contrast becomes sensitive to the number of atomic layers.

Graphene and multilayers graphene samples are perfect candidates for imaging with the use of SE1 and BSE electrons in SEM at low kV operation, and the other way round: low kV SEM seems to be a perfect tool for graphene imaging. What it takes, is the ability of the operator to apply optimum imaging conditions and be able to serve with reasonable interpretation of the images after all. That causes SEM not only a tool for imaging, but rather a system for research application.

The typical scanning electron microscopy images of graphene grown on copper foil recorded at primary beam energy of 0.5 keV are presented in Fig.1.

Image in Fig. 1a reveals the presence of cracks in the graphene sheet, which most probably are generated during the cooling of the sample after the growth process. The bare copper in this region has been oxidized after the contact with air, and appears as bright lines in the image (red arrows). The same cracks are represented by dark lines in the image of BSE (compare Fig. 1b). However, there are many more dark lines visible in the BSE image (yellow arrows), which originate from the folds of the graphene sheet on the copper surface. The presence of the folds is the result of differences in the thermal expansion coefficient of Cu substrate and graphene sheet. Both, cracks and folds, appear dark in the BSE image, thus it would not be possible to differentiate between them, unless the SE1 image was recorded in parallel with the BSE image. In many cases of the results concerning the graphene imaging by SEM, which can be found in the literature, the authors rely on the BSE or SE2 (SE type 2) images to acquire information on the graphene structures. In the outcome, some of the features of graphene sheets may be

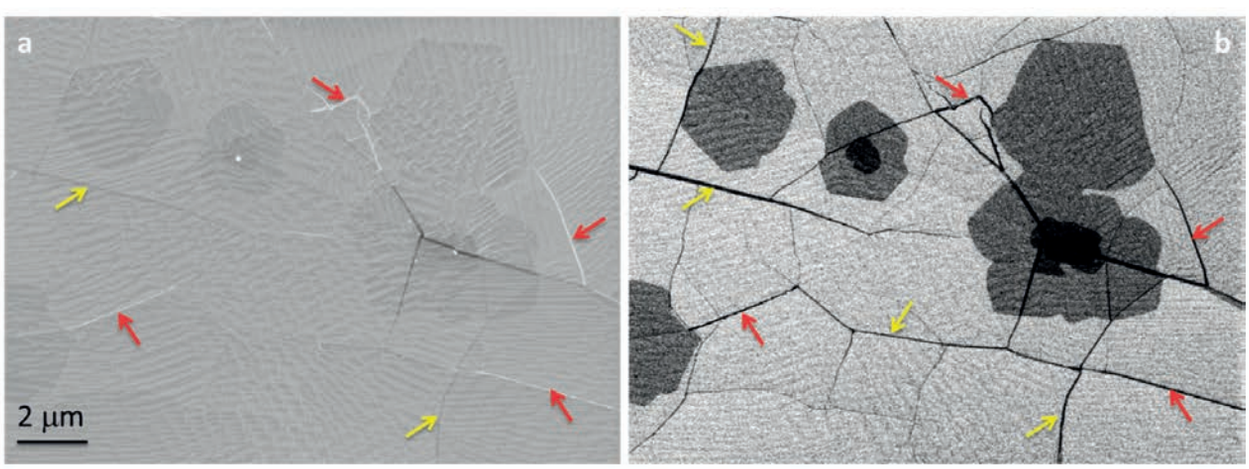

Fig. 1. SEM images of graphene grown over the Cu substrate: (a) – SE1 image, (b) – BSE image; cracks and folds in graphene sheet marked with red and yellow arrows, respectively.
Rys. 1. Obrazy SEM grafenu na podłożu Cu: (a) – obraz SE1, (b) – obraz BSE; pęknięcia i fałdy w warstwie grafenu oznaczono odpowiednio czerwonymi i żółtymi strzałkami.

misinterpreted [18, 20]. Only by comparative analysis of the two images taken at the same time in two channels (SE1 and BSE) it is possible to determine the origin of individual lines in the BSE image, as presented herein.

Similarly, it is necessary to perform image recording in a dual-channel mode to see other features typical for the CVD-grown graphene over a Cu substrate, i.e. add-layers. The add-layers are hardly visible in the SE1 image, but they can be clearly seen in the BSE image. The contrast is governed by the changes in the thickness of the graphene sheet over the substrate, namely the number of add-layers.

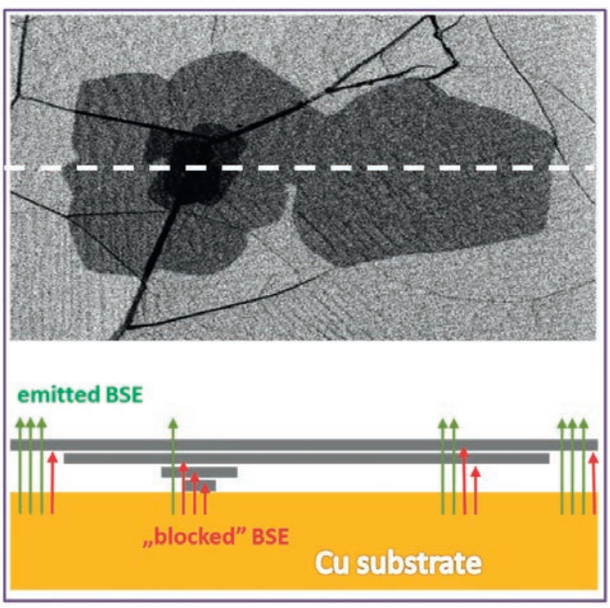

Fig. 2. Schematic representation of thickness contrast mechanism in LL-BSE image of graphene on Cu substrate (not in scale).
Rys. 2. Schematyczna reprezentacja mechanizmu kontrastu w LL-BSE związanego ze zmianą liczby warstw grafenu na podłożu Cu (nie w skali).

A reduction in the landing energy will result in smaller electron penetration depth and hence more information of interest will come from the surface [21]. By definition and because of the physical processes, the low-loss BSE must come from the outermost layers of the surface. The greater discrimination applied with the filtering grid to the smallest energy loss possible, the more the detection signal originates from the surface layers. Using this principle, the thinnest films on the surface, down to monolayers, can be imaged. In the case considered, most of the BSE are still generated within the Cu foil (Fig. 2). The reduction of the net signal to the smallest energy losses increases the contrast dramatically. At such circumstances, even the presence of additional single atomic layer on the surface (single add-layer) becomes a serious obstacle for the BSE on their way to the detector. Thus the regions of the sample covered with additional layers will be represented by the decreased intensity of BSE signal, i.e. dark parts in the image. In case of graphene on Cu, these will be discrete changes, thus informing about the number of layers. The proposed description of thickness contrast mechanism in LL-BSE images is also applicable to folds of graphene sheet, which in fact can be considered as local increase in the number of layers.

It is worth to note, that add-layers (schematically shown in Fig. 2) are placed below the continuous sheet of graphene. This finding has been previously reported by [22 - 23] and is widely accepted by the technologists.

Another interesting feature present in the low-kV BSE images of graphene on Cu is the contrast observed

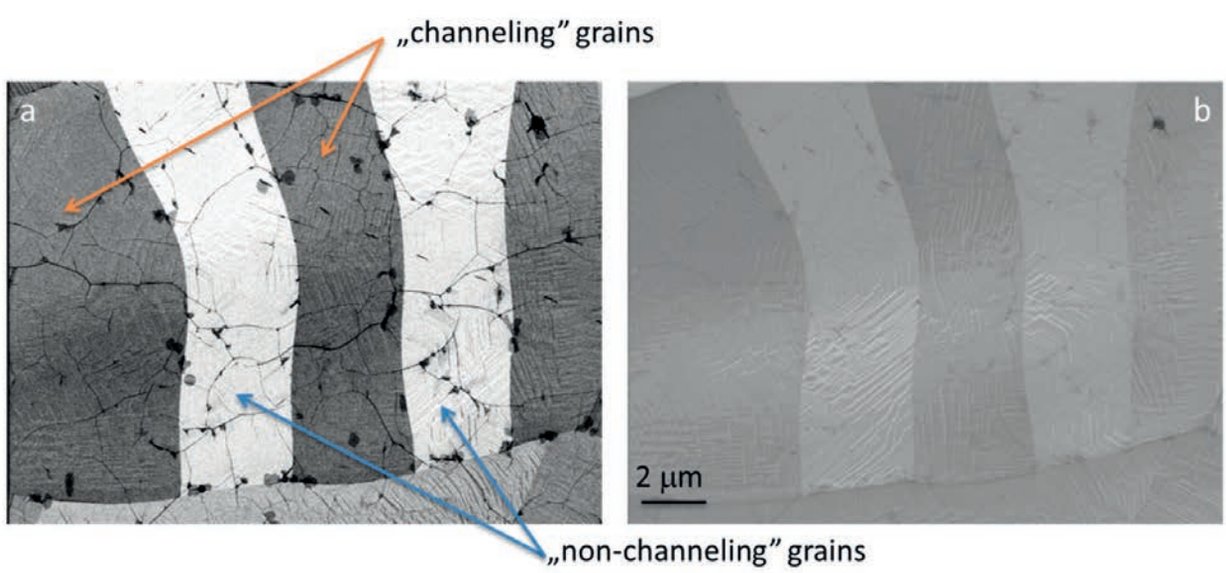

Fig. 3. Channeling contrast in the Cu grains under graphene clearly visible in BSE image: (a) channeling grains appear darker than non-channeling grains; (b) SE1image of the same fragment of the sample: weak channeling contrast.
Rys. 3. Kontrast kanałowania elektronów w polikrystalicznym podłożu Cu pokrytym grafenem widoczny w obrazie BSE: (a): ziarna kanałujące jawią się jako ciemniejsze niż ziarna niekanałujące; (b) obraz SE1 tego samego fragmentu próbki: słaby kontrast kanałowania.

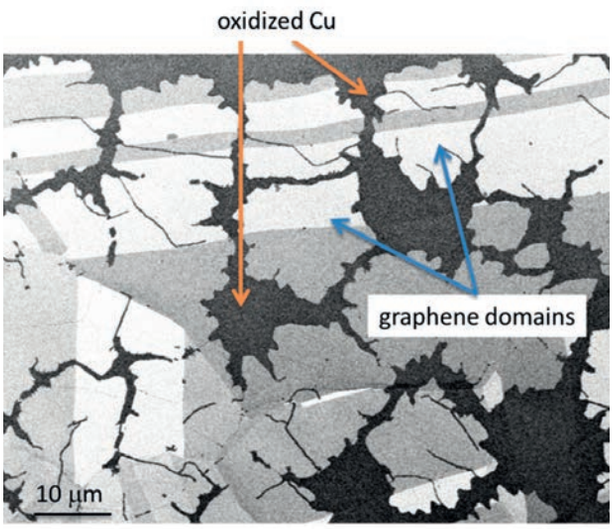

Fig. 4. SEM image (BSE) of the initial phase of graphene growth over polycrystalline Cu substrate; channeling contrast is observed only in the regions covered with graphene, in contrary to the fragments of oxidized Cu.
Rys. 4. Obraz SEM (BSE) grafenu na podłożu Cu we wczesnej fazie wzrostu; kontrast kanałowania obserwowany tylko w obszarach pokrytych grafenem, w przeciwieństwie do fragmentów utlenionej Cu.

for the Cu grains in polycrystalline substrate. The value of the backscattering coefficient in the individual grains of material is orientation-dependent [24]. The scattering is lowest for the grains which main crystallographic axis is aligned with the primary beam direction, and so is the intensity of BSE signal.

The strongly-misoriented grains are characterized by high scattering coefficient, thus the signal registered in the BSE image over such grains is very strong (Fig. 3). Analogous, however much weaker, contrast can be observed in SE1 image as well. In this case the signal intensity is more dependent on the work function of electrons from the individual grains (Fig. 3b).

The type of contrast described above, called channeling contrast, can be observed at low primary beam energies only when the surface of the studied sample is crystalline, free from defects, oxides and perfectly clean. Coverage of the copper surface with graphene ensures that all of these requirements are fulfilled. The best example of the antioxidant properties of the graphene on the metallic substrate can be observed in the image of the sample in the initial phase of growth, when the graphene forms micro--domains. In contrast to the parts of Cu surface covered with graphene, oxidized (by the contact with air) fragments of copper do not present any contrast in-between the individual grains.

In order to find optimum set of the primary electron beam parameters suitable for graphene on Cu observation, the series of images was recorded in parallel mode (SE1 and BSE simultaneously) with an application of beam energies ranging from 0.5 keV to 10 keV. Fig. 5 presents a set of images registered for the same fragment of the sample at different imaging conditions.

Typical features of the graphene film on Cu substrate, such as folds, cracks in graphene foil and add-layers, are visible in all of the SE1 images even at the beam energy as high as 10 keV (Fig. 5a – e). Despite the fact, that all the features are visible in the image at 10 keV (Fig. 5e), the information they bring may be misinterpreted, as both, cracks and folds appear to be alike. From the images presented in Fig. 5, only the one registered at 0.5 keV-beam operation allows to clearly distinguish between aforementioned features (Fig. 5a). On the other

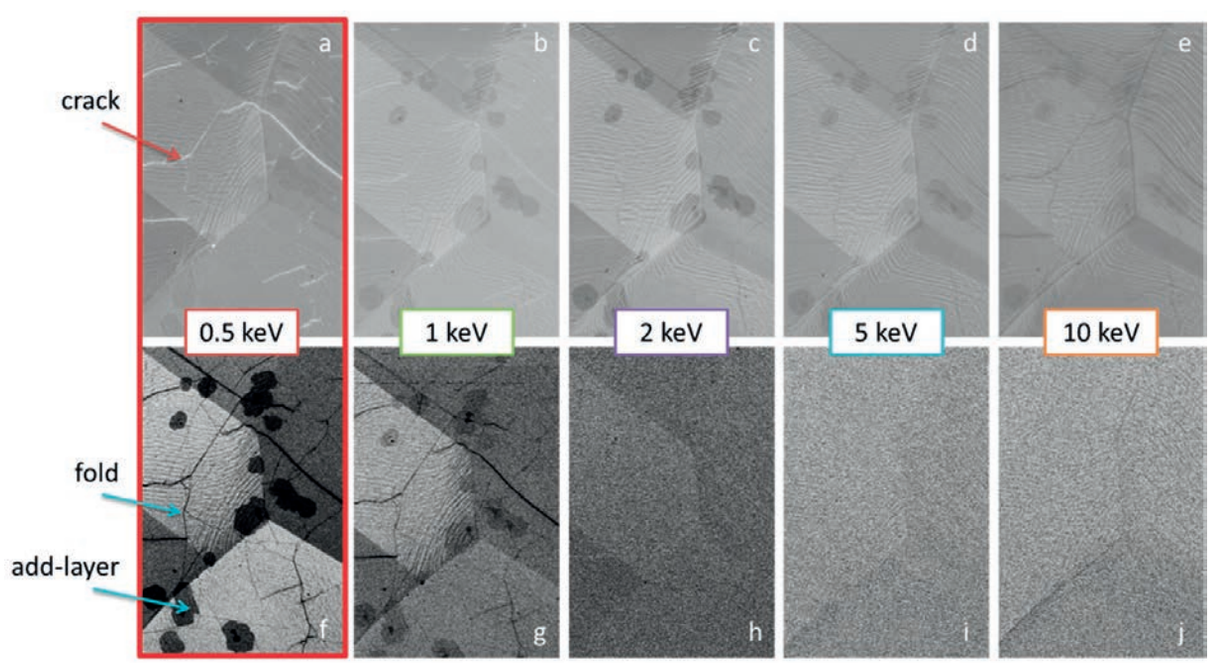

Fig. 5. Set of SE1 and BSE images of graphene grown on Cu, obtained at different values of energy of primary electron beam.
Rys. 5. Obrazy SE1 i BSE grafenu na podłożu Cu, uzyskane przy różnych wartościach energii elektronów pierwotnych.

hand, SEM imaging in a single mode (SE1 either BSE) is insufficient to gather full available information about the sample. The add-layers are not (or hardly) visible in the SE1 mode at 0.5 keV. That is why it is necessary to perform double-channel signal registration during SEM imaging (SE1 and BSE). At the primary beam energy above 1 keV, the BSE images contain no useful information on the graphene on the Cu substrate, only residual information on the existence of grains in the substrate. That is caused by the loss of information delivered by the BSE which encounter multiple Rutherford scattering and their increased penetration depth. Only by the application of low energy of the primary beam and selection of the low-loss BSE from the remainder of the whole electron spectrum it becomes possible to limit the information which originates from the outermost shallow region on the surface.

4. Summary and conclusions

The SEM imaging must be performed in such a way, that images collected will provide as much information about the studied sample as possible. One of the fundamental conditions is to optimize microscope settings and to give reasonable interpretation of the images. That is why understanding the contrast in the recorded images is so important. The samples studied in this work were the layers of graphene obtained by CVD method on Cu substrates. The influence of SEM imaging conditions on the quality of information gathered by this technique has been considered. The results of this study demonstrate undeniably high utility of low energy scanning electron microscopy in the observation and characterization of graphene layers on various substrates. The advantages of SEM technique are: it is fast, non-destructive, non--contact, allowing for examination of relatively vast areas on the sample, and there is no need of special sample preparation. High-resolution SEM imaging makes it much more precise method of characterization in terms of features which become "invisible" for other techniques, i.e. Raman spectroscopy due to poor resolution of the latter. The practical aspect of the work presented here is the development of a novel method of low-kV SEM characterization of thin materials, which will serve as a rapid characterization tool of graphene layers obtained in the laboratory, and can be used for graphene produced on an industrial scale, as well.

Acknowledgment

Author would like to thank Dr. Iwona Pasternak (Institute of Electronic Materials Technology, Poland) for preparation of graphene samples used in this study. This work was partially sponsored by the Polish Ministry of Science and Higher Education, in the frame of the research project entitled „Examination of graphene by SEM in terms of the identification of the numbers of graphene layers" held at the Institute of Electronic Materials Technology.

References

[1] Bae S., Kim H., Lee Y., Xu X., Park J. - S., Zheng Y., Balakrishnan J., Lei T., Kim H. R., Song Y. I., Kim Y. - J., Kim K. S., Ozyilmaz B., Ahn J. - H., Hong B. H., Iijima S.: Roll-to-roll production of 30-inch graphene films for transparent electrodes, *Nature Nanotechnology*, 2010, 5, 574 – 578

[2] Reina A., Son H., Jiao L., Fan B., Dresselhaus M. S., Liu Z. F., Kong J.: Transferring and identification of single - and few-layer graphene on arbitrary substrates, *J. Phys. Chem. C,* 2008, 112 (46), 17741 – 17744

[3] Geim A. K.: Graphene: Status and prospects, *Science*, 2009, 324, 1530 – 1534

[4] Zhang Y., Tan Y. - W., Stormer H. L., Kim P.: Experimental observation of the quantum Hall effect and Berry's phase in graphene, *Nature,* 2005, 438, 201–204

[5] Blake P., Hill E. W., Castro Neto A. H., Novoselov K. S., Jiang D., Yang R., Booth T. J., Geim A. K.: Making graphene visible, *Appl. Phys. Lett*., 2007, 91, 63124

[6] Gao L., Ren W., Li F., Cheng H. M.: Total color difference for rapid and accurate identification of graphene, *ACS Nano,* 2008, 2, 1625 – 33

[7] Nair R. R., Blake P., Grigorenko A. N., Novoselov K. S., Booth T. J., Stauber T., Peres N. M. R., Geim A. K.: Fine structure constant defines visual transparency of graphene, *Science*, 2008, 320, 1308

[8] Almeida C. M., Carozo V., Prioli R., Achete C. A.: Identification of graphene crystallographic orientation by atomic force microscopy, *J. Appl. Phys*., 2011, 110, 086101

[9] Hass J., de Heer W. A., Conrad E. H.: The growth and morphology of epitaxial multilayer graphene, *J. Phys.*: *Condens. Matter,* 2008, 20, 323202

[10] Ferrari A. C., Meyer J. C., Scardaci V., Casiraghi C., Lazerri M., Mauri F., Piscanec S., Jiang D., Novoselov K. S., Roth S., Geim A. K.: Raman Spectrum of Graphene and Graphene Layers, *Phys. Rev. Letters,* 2006, 97, 187401

[11] Ferrari A. C.: Raman spectroscopy of graphene and graphite: Disorder, electron–phonon coupling, doping and nonadiabatic effects, *Solid State Comm*., 2007, 143, 47 – 57

[12] Meyer J. C.: Transmission electron microscopy (TEM) of graphene, Graphene, Woodhead Publishing

Limited, Amsterdam, 2014, 101 – 123

[13] Sawada H., Sasaki T., Hosokawa F., Suenaga K.: Atomic - resolution STEM imaging of graphene at low voltage of 30 kV with resolution enhancement by using large convergence angle, *Phys. Rev. Lett.* 2015, 114, 166102

[14] Krauss B., Lohmann T., Chae D. - H., Haluska M., von Klitzing K., Smet J. H.: Laser - induced disassembly of a graphene single crystal into a nanocrystalline network, *Phys. Rev. B,* 2009, 79, 165428

[15] Xu M., Fujita D., Gao J., Hanagata N.: Auger electron spectroscopy: A rational method for determining thickness of graphene films, *ACS Nano,* 2010, 4(5), 2937 – 2945

[16] Hiura H., Miyazaki H., Tsukagoshi K. : Determination of the number of graphene layers: discrete distribution of the secondary electron intensity stemming from individual graphene layers, *Appl. Phys. Express,* 2010, 3, 095101

[17] Kochat V., Pal A. N., Sneha E. S., Sampathkumar A., Gariola A., Shivashankar S. A., Raghavan S., Ghosh A.: High contrast imaging and thicnkess determination of graphene with in-column secondary electron microscopy, *J. Appl. Phys*., 2011, 110, 014315

[18] Lee J., Zheng X., Roberts R. C., Feng P. X. - L.: Scannning electron microscopy characterization of structural features in suspended and non-suspended graphene by customized CVD growth, *Diam. Relat. Mater*. 2015, 54, 64

[19] Xie J., Spallas J.: Layer number contrast of CVD--derived graphene in low voltage scanning electron microscopy, Microsc. *Microanal.* 2013, 19 (Suppl 2), 370

[20] Zhou Y., Fox D. S., Magiure P., O'Connel R., Masters R., Rodenburg C., Wu H., Dapor M Chen Y., Zhang H.: Quantitative secondary electron imaging for work function extraction at atomic level and layer identification of graphene, *Sci. Rep*., 2016, 6, 21045.

[21] Reimer L.: Scanning electron microscopy, second ed., Springer Verlag, Berlin, 1998

[22] Li Q., Chou H., Zhong J. - H., Liu J. - Y., Dolocan A., Zhang J Zhou Y., Ruoff R. S., Chen S., Cai W.: Growth of adlayer graphene on Cu studied by carbon isotope labeling, *Nano Lett*., 2013, 13(2), 486 – 490

[23] Nie S., Wu W., Xing S., Yu Q., Bao J., Pei S. -S., McCarty K. F.: Growth from below: bilayer graphene on copper by chemical vapor deposition, *New J. Phys.,* 2012, 14, 093028

[24] Reimer L.: Image formation in low-voltage scanning electron microscopy, SPIE Tutorial Texts in Optical Engineering, Vol. TT12, Bellingham, WA, 1993

Stabilność wysokotemperaturowa ekologicznych rezystorów grubowarstwowych

Konrad Kiełbasiński[1], Jerzy Szałapak[1, 2], Jakub Krzemiński[2], Anna Młożniak[1], Małgorzata Jakubowska[1, 2], Sławomir Szostak[3]

[1] Instytut Technologii Materiałów Elektronicznych
ul. Wólczyńska 133, 01 - 919 Warszawa
e-mail: konrad.kielbasinski@itme.edu.pl

[2] Wydział Mechatroniki, Politechnika Warszawska
ul. św. Andrzeja Boboli 8, 02 - 525 Warszawa

[3] Instytut Mikroelektroniki i Optoelektroniki, Politechnika Warszawska
Koszykowa 75, 00 - 662 Warszawa

Streszczenie: W związku z Dyrektywą RoHS, która weszła w życie w 2006 roku producenci materiałów elektronicznych zostali zmuszeni do wyeliminowania m.in. ołowiu i jego związków ze składów tych materiałów. Dyrektywa wymusiła zmianę składu past służących do wytwarzania rezystorów grubowarstwowych szeroko rozpowszechnionych w konsumenckim sprzęcie elektronicznym. Autorzy zaproponowali nowatorskie pasty rezystywne zdolne w pełni zastąpić pasty oparte o ołów i jego związki. Ponadto zostały przeprowadzone badania odporności na narażenia termiczno-prądowe, które ujawniły przewagę użytkową w aspektach stabilności rezystancji na cykliczne narażenia temperaturowe nowych past wobec past tradycyjnych.

Słowa kluczowe: rezystory bezołowiowe, stabilność wysokotemperaturowa

High temperature stability of eco-friendly thick-film resistors

Abstract: Under the EU directive on the Restriction of Hazardous Substances (RoHS) implemented in 2006, producers of electronics materials were obliged to eliminate lead and its compounds from the compsition of their products. As a consequence of this directive the changes affected the compositions of pastes used in the production of thick-film resistors, widely used in mass electronics. The authors have developed new compositions for the resistive thick film pastes, to replace the ones based on lead. Moreover, the thermal and electrical studies showed the advantage of the new compositions over the traditional ones in terms of resistance stability under temperature cyclic test.

Key words: lead-free resistors, high temperature stability

1. Wstęp

Technologia grubowarstwowa jest dominującą technologią wytwarzania podzespołów biernych. Ważnym podzespołem jest rezystor zaprezentowany na Rys. 1, który składa się z warstw przewodzącej i rezystywnej nanoszonych sitodrukiem na ceramiczne podłoże, a następnie wypalanych w temperaturze dochodzącej do 600 - 900°C. W strukturze warstwy rezystywnej można wyróżnić ziarna fazy funkcjonalnej oraz szkliwo.

Faza funkcjonalna rezystorów tradycyjnych to w przeważającej większości mieszanina proszków rutenianu ołowiu i rutenianu bizmutu wykrystalizowanych w strukturze pirochloru. W rezystorach niskorezystywnych stosowany jest dwutlenek rutenu. Natomiast szkliwo to mieszanina tlenku ołowiu, boru i krzemu.

Tlenek ołowiu pozwala na kontrolę rozszerzalności warstwy rezystywnej umożliwiając dopasowanie współczynnika rozszerzalności warstwy rezystywnej do podłoża. Ponadto jego dodatek zmniejsza temperaturowy współczynnik lepkości w zakresie temperatur 750 ÷ 900°C [1] oraz zapewnia odporność warstwy na oddziaływanie wody i czynników chemicznych.

Tlenek ołowiu, w zależności od jego koncentracji, może pełnić w szkliwie funkcję modyfikującą oraz szkłotwórczą. Cheng i współpracownicy zbadali wpływ proporcji składników PbO i B_2O_3 na tworzenie się szkła i zaobserwowali, że dla zawartości PbO poniżej 20% molowych struktura szkliwa przypomina strukturę utworzoną przez czysty tlenek boru [2]. Tlenek ołowiu pełni jedynie funkcję modyfikatora, a szkliwo jest niestabilne – pojawia się w nim niepożądana faza krystaliczna. Podczas chłodzenia zachodzi krystalizacja powierzchniowa i objętościowa. Zwiększanie zawartości tlenku ołowiu w zakresie od 30 do 60% powoduje zmianę przestrzennej struktury anionów borowych z $[BO_3]^{3-}$ na $[BO_4]^{5-}$. Nasilenie tego zjawiska jest proporcjonalne do zawartości tlenku ołowiu. Szkliwo w tym zakresie składów jest klarowne – nie ulega krystalizacji. Powyżej 60% zawartości PbO tworzą się łańcuchy B-O-Pb, co dowodzi szkłotwórczej roli tlenku ołowiu powyżej tej zawartości.

Tlenek ołowiu zawarty w szkliwie reaguje ze związkami rutenu w czasie wypalania, modyfikując wartości rezystancji i temperaturowego współczynnika rezystancji (TWR). W wypalanych warstwach rezystywnych zawiera-

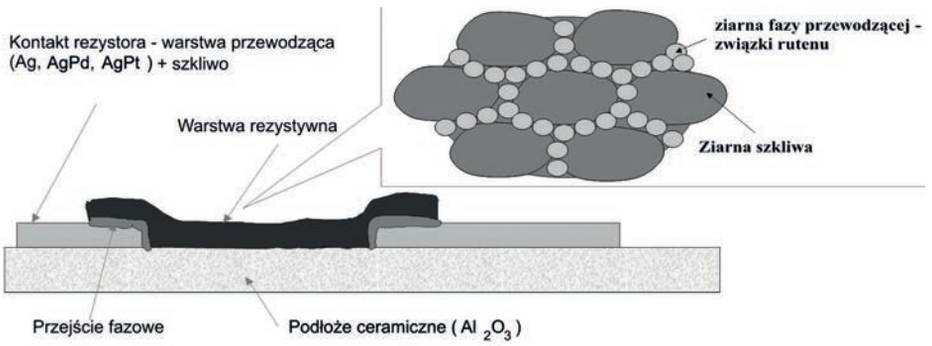

Rys. 1. Model struktury rezystora grubowarstwowego.
Fig. 1. Thick-film resistor's structural model.

jących rutenian bizmutu przy współudziale tlenku ołowiu, zachodzi reakcja wymiany bizmutu i ołowiu pomiędzy tlenkiem i rutenianem, opisana wzorem:

$$Bi_2Ru_2O_7 + 2PbO \leftrightarrow Pb_2Ru_2O_6 + Bi_2O_3 \qquad (1)$$

Występowanie reakcji zostało udowodnione przez Mortena i in. na podstawie badań past rezystywnych DP 1441, bazujących na rutenianie bizmutu i szkliwie zawierającym m.in. tlenek ołowiu [3]. Morten dokonał porównania stałej sieciowej niewypalonej i wypalonej warstwy rezystywnej za pomocą rentgenografii strukturalnej (*X-Ray Diffraction – XRD*) i elektronowego mikroskopu skaningowego (S*canning Electrone Microscope – SEM*) z EDS (*Energy Dispersive X-Ray Spectroscopy*). Po wypaleniu warstwy, zmianie ulega stała sieciowa rutenianu z wartości 10,3 Å, charakterystycznej dla $Pb_2Ru_2O_7$, na wartość 10,28 Å, będącą pośrednią pomiędzy rutenianem bizmutu i ołowiu. Ponadto przeprowadzona analiza EDS dowiodła zachodzenia zmian w proporcjach ołowiu i rutenu w ziarnach szkliwa. Pike i Seager przewidzieli występowanie reakcji wymiany ołowiu i bizmutu pomiędzy szkliwem i fazą funkcjonalną na podstawie zmian w temperaturowym współczynniku rezystancji, który utrzymywał się na stałym poziomie pomimo zwiększania temperatury wypalania [4].

W wypalanych warstwach opartych na dwutlenku rutenu, zawierających szkliwo o istotnej zawartości ołowiu, może zachodzić reakcja syntezy zgodnie ze wzorem:

$$2RuO_2 + 2PbO\ (szkliwo) \rightarrow Pb_2Ru_2O_6 \qquad (2)$$

Kuiel i in. przeprowadzili analizę XRD, która wykazała, że dwutlenek rutenu w warunkach wypalania rezystora, reaguje ze szkliwem zawierającym istotną ilość tlenku ołowiu, w wyniku czego powstaje rutenian ołowiu [5]. Stopień przereagowania dwutlenku rutenu jest wprost proporcjonalny do temperatury wypalania.

Reakcje (1 - 2), w których powstaje rutenian ołowiu, mają ogromne znaczenie praktyczne. Beyerlein i in. [6] wykazali, że wraz ze zwiększaniem się proporcji liczby atomów ołowiu do liczby atomów bizmutu w rutenianie stopniowo maleje temperaturowy współczynnik rezystancji (TWR), osiągając wartość zerową przy proporcji molowej Bi do Ru na poziomie około 20%. Jest to spowodowane przemianą rutenianu bizmutu w rutenian ołowiu, skutkującą obniżeniem TWR fazy przewodzącej z + 1100 ppm/°C do + 100 ppm/°C.

Przemiana dwutlenku rutenu w rutenian ołowiu również powoduje obniżenie TWR fazy przewodzącej zawartej w warstwie z + 5600 ppm/°C do wartości + 100 ppm/°C. Ułatwia to uzyskanie rezystorów o wysokiej rezystancji, o temperaturowych współczynnikach rezystancji w granicach ± 200 ppm/°C

W wypalanej warstwie, pod wpływem temperatury zachodzi też proces spiekania o przeciwstawnym wpływie na rezystancję w stosunku do reakcji przemiany fazy przewodzącej. Na skutek spiekania ziarna fazy przewodzącej ulegają zagęszczeniu, w wyniku czego następuje obniżanie się rezystancji oraz zwiększanie się TWR, postępujące w miarę wydłużania czasu lub podwyższania temperatury wypalania. Dwa procesy, wpływające przeciwstawnie na rezystancję i TWR zachodzą równocześnie. Zjawisko to, badane m.in. przez Kuiela [5] umożliwia uzyskanie rezystorów, których rezystancja i TWR są mało wrażliwe na warunki wypalania, o ile wzajemne szybkości zachodzenia procesów spiekania i przemiany fazy funkcjonalnej w rutenian ołowiu są kontrolowane.

Dyrektywa RoHS (*Restriction of Hazardous Substances*), wprowadzona w 2006 roku, ograniczyła stosowanie niebezpiecznych substancji, w tym ołowiu i kadmu. Firmy Du Pont oraz ESL od 2006 r. oferują bezołowiowe pasty rezystywne, ale ich zakres rezystancji powierzchniowej wynosi 1 ÷ 10 Ω/□ i jest zbyt wąski na potrzeby współczesnych urządzeń elektronicznych. Pasty o wyższych rezystancjach są oferowane w technologii niezgodnej z RoHS. W istniejących doniesieniach literaturowych badacze opisują niestabilność rezystancji oraz wysokie wartości temperaturowych współczynników rezystancji wytwarzanych rezystorów bezołowiowych.

Celem opisanych badań jest porównanie stabilności wysokotemperaturowej klasycznych rezystorów grubowarstwowych z bezołowiowymi, wykonanymi z nowatorskich past rezystywnych. Zaproponowane pasty rezystywne są oparte na dwutlenku rutenu, szkliwie bezołowiowym oraz nośniku organicznym. Są one przed-

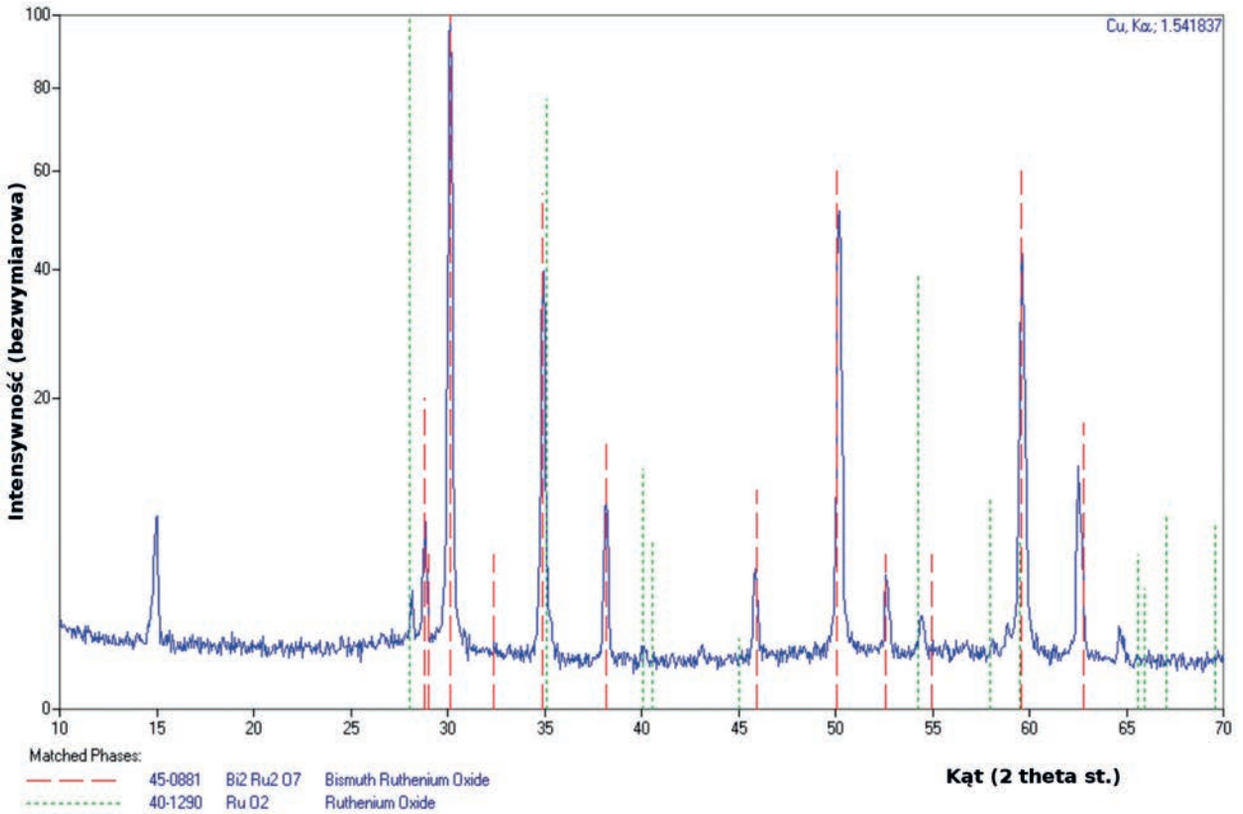

Rys. 2. Dyfraktogramy proszku Bi_2RuO_7 prod. Mennicy Państwowej.
Fig. 2. Diffraction patterns of powder Bi_2RuO_7 produced by Polish National Mint.

miotem prac badawczych prowadzonych od 2004 roku, które w 2006 roku zaowocowały uzyskaniem past rezystywnych pokrywających zakres rezystancji od 10 do 1000 Ω/□ [7], natomiast w 2008 roku zakres rezystancji uległ zwiększeniu do 10 Ω/□ ÷ 100 kΩ/□ [8], tym samym zaspokajając w przeważającej części zapotrzebowanie rynkowe na zakres rezystancji past rezystywnych. Rezystancja i temperaturowy współczynnik rezystancji nie są jedynymi cechami rezystorów grubowarstwowych. Z punktu widzenia producenta sprzętu elektronicznego, w szczególności do zastosowań medycznych i militarnych, równie istotna jest stabilność rezystancji podczas narażeń prądowych i termicznych, czym autorzy motywują podjęcie tematu.

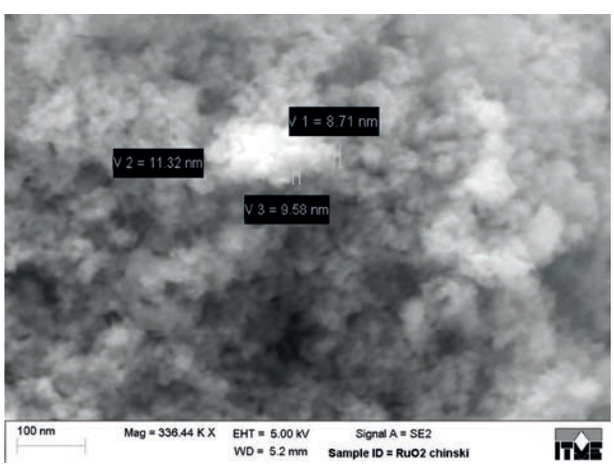

Rys. 3. Zdjęcie SEM proszku RuO_2 prod. Chemlin z dokonanymi pomiarami średnic ziaren.
Fig. 3. SEM image of powder RuO_2 produced by Chemlin with grain diameter measurements.

2. Wytworzenie próbek testowych

2.1. Wybór fazy funkcjonalnej

Pierwszym zastosowanym proszkiem był rutenian bizmutu wytworzony przez Mennicę Państwową zgodnie z Warunkami Technicznymi R-42. Badania wykonane metodą dyfrakcji rentgenowskiej (XRD) wskazują na strukturę pirochloru o wzorze chemicznym $Bi_2Ru_2O_7$. Jest to typowy proszek stosowany w klasycznych pastach rezystywnych.

Drugim zastosowanym materiałem był tlenek rutenu RuO_2 – również w postaci proszku, z firmy Chemlin (Nanjing Chemlin Chemical Industry Co., Ltd.), charakteryzowany na podstawie obserwacji SEM, pomiaru powierzchni właściwej metodą Brunauera – Emmetta – Tellera (BET) oraz mikroanalizy XRD. Na zdjęciu SEM zamieszczonym na Rys. 3 zidentyfikowano drobne ziarna o wielkości około 10 nm. W celu sprawdzenia czystości proszku wykorzystano analizę EDS (*Energy Dispersive*

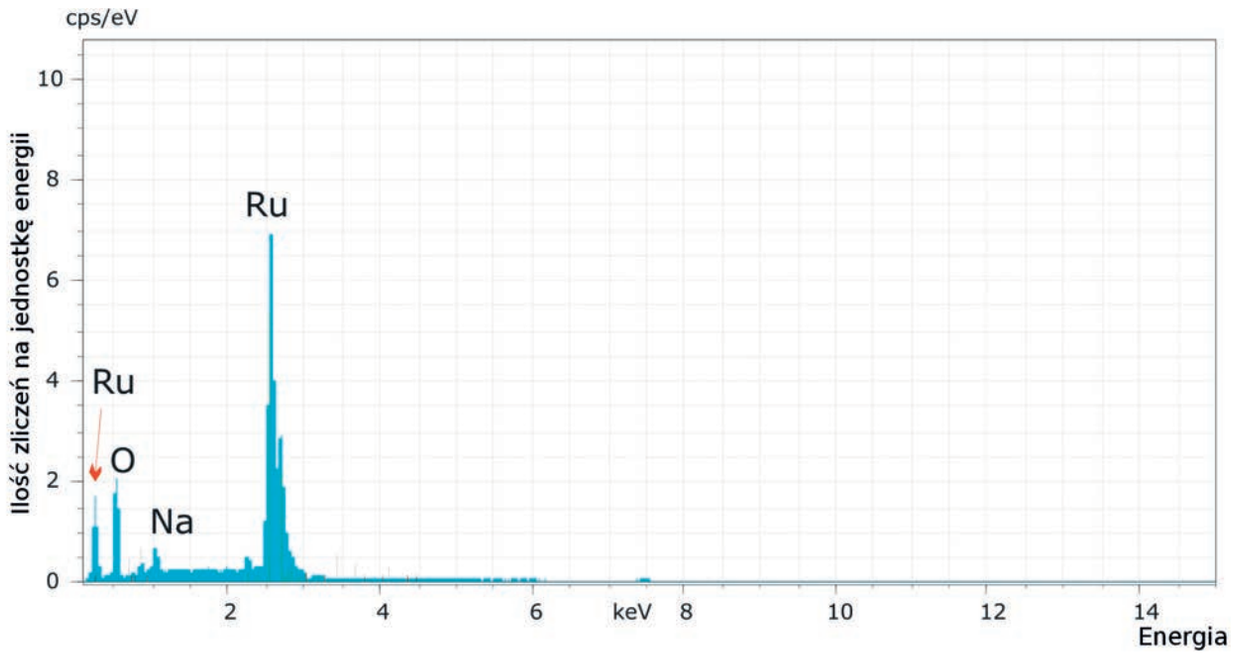

Rys. 4. Analiza EDS proszku RuO_2 prod. Chemlin.
Fig. 4. EDS analysis of RuO_2 powder, produced by Chemlin.

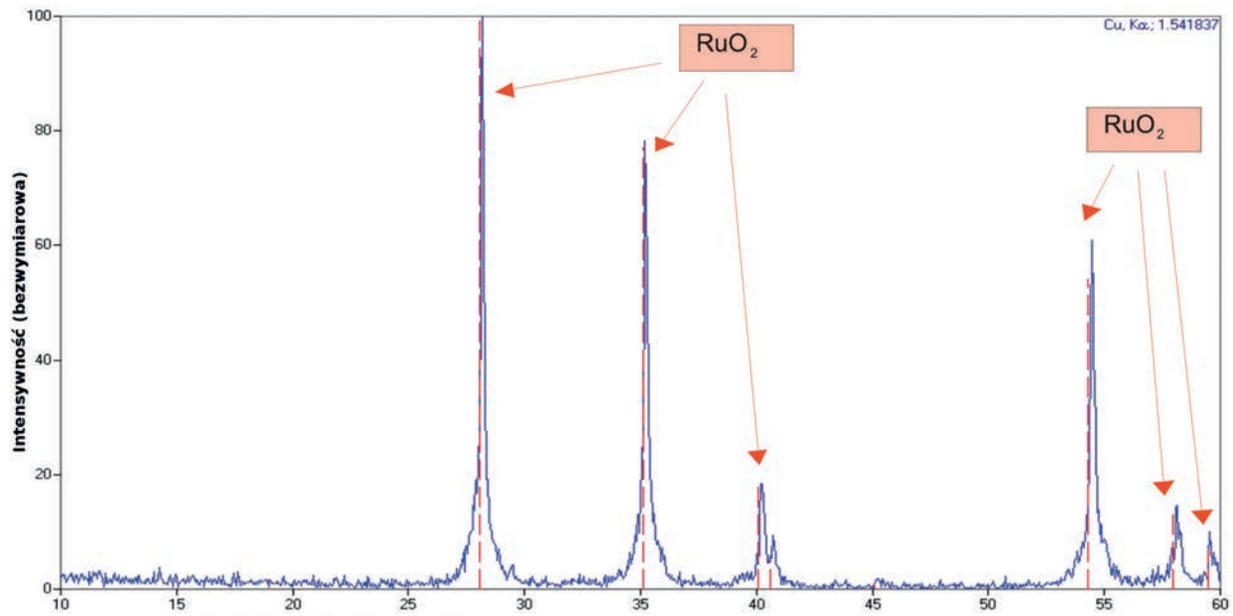

Rys. 5. Dyfraktogramy proszku RuO_2 prod. Chemlin.
Fig. 5. Diffraction patterns of powder RuO_2 produced by Chemlin.

X-Ray Spectrometer). Rezultaty przedstawiono na Rys. 4. Wykryto w nim zanieczyszczenia w postaci sodu (tlenku sodu) będącego najprawdopodobniej pozostałością po ługu sodowym, używanym w reakcji strącania $RuCl_3$ do RuO_2. Stwierdzony poziom zanieczyszczenia proszku tlenkiem sodu nie stanowi zagrożenia funkcjonowania rezystora. Tlenek sodu podczas wypalania rozpuszcza się w objętości szkliwa, podnosząc nieznacznie poziom Na_2O obecnego w szkliwie bezołowiowym. Pomiar powierzchni właściwej metodą BET wykazał wartość ok 50 m^2/g, co odpowiada średniemu uziarnieniu na poziomie 10 nm.

W celu zweryfikowania struktury krystalicznej badanych proszków oraz wyznaczenia średniego rozmiaru krystalitu z użyciem wzoru Shrererra wykonano pomiary proszku fazy funkcjonalnej metodą dyfrakcji rentgenowskiej XRD. Zbadano proszek Bi_2RuO_7 pochodzący z Mennicy Państwowej (Rys. 2) oraz RuO_2 z firmy Chemlin (Rys. 5). Kształt refleksów dyfrakcyjnych proszku Chemlin wskazuje na występowanie dwóch frakcji krystalitów: drobnej o uziarnieniu 10 nm i grubej o uziarnieniu 100 nm. W obu proszkach stwierdzono występowanie silnych refleksów dla kątów „2 θ" równych 28,12°, 35,15°, 54,39°,

które odpowiadają stałym sieci równym odpowiednio: 3,17 Å, 2,55 Å, 1,68 Å dla trzech kierunków krystalograficzych: [1 1 0], [1 0 1], [2 1 1]. Zbliżone położenia refleksów zaobserwowali Pflieger i in. [9].

Każda z użytych metod pomiarowych pozwoliła wykazać, że proszek RuO_2 firmy Chemlin charakteryzuje się znacznym udziałem drobnych ziaren RuO_2.

2.2. Wybór szkliwa

Zaproponowano 3 rodzaje szkliw, w tym dwa bezołowiowe SzR-16 (Pb-free), SzR-10 (Pb-free) oraz jedno ołowiowo-boro-glino-krzemowe o oznaczeniu F0-36, stosowane w tradycyjnej serii past rezystywnych ITME R-300. Składy szkliw przedstawiono w Tab. 1.

Opracowanie składów szkliw bezołowiowych SzR-10 i SzR-16 było przedmiotem wcześniejszych prac badawczych [10]. Kryteriami doboru szkliw było dopasowanie współczynnika rozszerzalności cieplnej szkliwa do podłoża ceramicznego, temperatury topnienia zbliżonej do temperatury wypalania oraz zdolności do kompensacji temperaturowego współczynnika rezystancji fazy przewodzącej RuO_2. Szkliwa poddano mieleniu w młynie planetarnym oraz sianiu do uzyskania średniego uziarnienia ok. 10 mikrometrów. Z proszku fazy funkcjonalnej, zmielonego szkliwa oraz nośnika przygotowano pastę. Proporcje składników suchych w przygotowywanych pastach zamieszczono w Tab. 2. Na każde 100 g składników suchych dodano 30 g nośnika organicznego będącego roztworem etylocelulozy w cellosolwie butylowym.

Składniki wstępnie zarabiano w moździerzu, a następnie poddano walcowaniu na trójwalcarce, uzyskując jednorodną pastę.

2.3. Procedura wytwarzania rezystorów

Płytkami podłożowymi była ceramika alundowa (Al_2O_3 96%) o grubości 0,635 mm, szerokości 25 mm i długości 38 mm. W pierwszym etapie na płytkę podłożową nanoszono warstwę kontaktów z komercyjnej pasty palladowo-srebrowej oznaczonej P-202 produkcji Instytutu Technologii Materiałów Elektronicznych. Naniesiona warstwa została wysuszona i wypalona. W drugim etapie nanoszono pastę rezystywną, którą wysuszono i wypalono. Metodą nanoszenia był powszechnie wykorzystywany sitodruk przez sito o gęstości 200 mesh. Grubości wysuszonych warstw przed wypaleniem wynosiły ok. 30 mikrometrów. Warstwy przewodzące i rezystywne były poddane kolejno tym samym procedurom suszenia i wypalania. Suszenie przeprowadzano przez 20 minut w 120°C. Warstwy wypalano w atmosferze powietrza w piecu tunelowym z zastosowaniem standardowego 1-godzinnego profilu wypalania warstw grubych o maksymalnej temperaturze 850°C z 10 minutowym czasem przetrzymania. Zdjęcie

Tab. 1. Składy opracowanych i zoptymalizowanych szkliw bezołowiowych w % mol.
Tab. 1. Compositions of investigated lead free glasses in molar %.

Symbol szkliwa	SiO_2	B_2O_3	PbO	CaO	Al_2O_3	BaO	MgO	K_2O	Na_2O	V_2O_5
Szkliwo zawierające tlenki litowców										
SzR-16 (Pb-free)	56	27	-	5,631	1,237	-	3,154	3,355	2,035	-
Szkliwo wolne od tlenków litowców										
SzR-10 (Pb-free)	43,5	35,0	-	-	9,3	7,8	-	-	-	4,5
Szkliwo ołowiowo-boro-glino-krzemowe										
F0-36	57,5	6,5	32,5	-	3,5	-	-	-	-	-

Tab. 2. Zawartość suchych składników past rezystywnych.
Tab. 2. Dry compound content of resistive pastes.

Oznaczenie pasty	SzR-16 % wag.	SzR-10 % wag.	$PbO-B_2O_3-SiO_2$ % wag.	RuO_2 % wag.	$Bi_2Ru_2RuO_7$	Rezystancja nominalna kΩ/□
R-100 Pbf	-	45	-	55		0,1
R-10k Pbf	65	-	-	35		10
R-200	-	-	30	-	70	0,2
R-5k	-	-	50	50		5

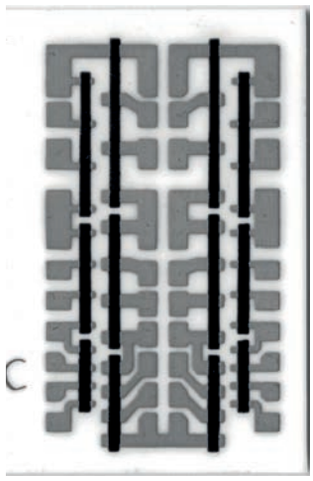

Rys. 6. Przykładowe zdjęcie próbki testowej przeznaczonej do termiczno – prądowych badań narażeniowych.
Fig. 6. A picture of a sample designed for thermal - current exposure tests.

jednej z wykonanych próbek przedstawiono na Rys. 6. Cechą wzoru jest ciągła ścieżka prądowa utworzona z 36 rezystorów o szerokości 1 mm oraz ich kontaktów. Taka koncepcja umożliwiająca jednoczesne poddanie narażeniom prądowym wszystkich rezystorów.

3. Pomiary

3.1. Opis stanowiska pomiarowego

Do badania charakterystyk temperaturowych zostały wykorzystane urządzenia z Instytutu Mikroelektroniki i Optoelektroniki Politechniki Warszawskiej. Instytut ten posiada urządzenie do pomiarów i narażeń prądowo-temperaturowych w zakresie temperatur od pokojowej do 500°C. Urządzenie zostało zautomatyzowane na potrzeby realizacji pracy. Stolik wyposażono w regulator temperatury ER 305 firmy EDO-Prudnik oraz w samodzielnie wykonany przez autorów liniowy układ sterowania mocą grzejną. Wbudowany w regulator algorytm sterowania PID oraz liniowe sterowanie grzaniem pozwoliły uzyskać stabilność temperatury na poziomie 1°C. Stolik był wyposażony w wolframowe sondy pomiarowe wraz z mikromanipulatorami (Rys. 7) oraz złącza typu BNC, wyprowadzające sygnały pomiarowe. Odpowiednie okablowanie zakończone gniazdami BNC oraz bananowymi umożliwiło podłączenie multimetru Keithley 2001 lub źródła pomiarowego Keithley 2400. Prezentowane stanowisko umożliwia zautomatyzowanie pomiarów do 20 rezystorów poprzez zastosowanie skanera Keithley 7011, który sekwencyjnie, na komendę przesłaną z oprogramowania PC interfejsem GPIB przełącza wejścia napięciowe multimetru na sondy napięciowe przyłożone do próbki.

Zastosowany regulator temperatury EDO 305 umożliwił komunikację z komputerem poprzez interfejs szeregowy w standardzie RS485 z użyciem protokołu komunikacyjnego MODBUS. W celu skomunikowania regulatora z komputerem PC zaprojektowano i zmontowano konwerter RS485 ↔ RS232.

Opracowano aplikację pomiarową, realizującą dwukierunkową komunikację pomiędzy regulatorem a PC w celu zadawania temperatury docelowej oraz odczytu aktualnej dla stolika grzejnego. W programie została zaimplementowana obsługa protokołu GPIB w celu odczytania wyników pomiaru z przyrządu Keithley 2400 lub Keithley 2001 oraz sterowania skanerem Keithley 7011. W rezultacie powstało stanowisko do pomiaru charakterystyk temperaturowych rezystorów metodami dwu- i czteropunktową. Program gromadzi dane o chwili czasu, zmierzonej temperaturze i wartości rezystancji, napięcia bądź prądu,

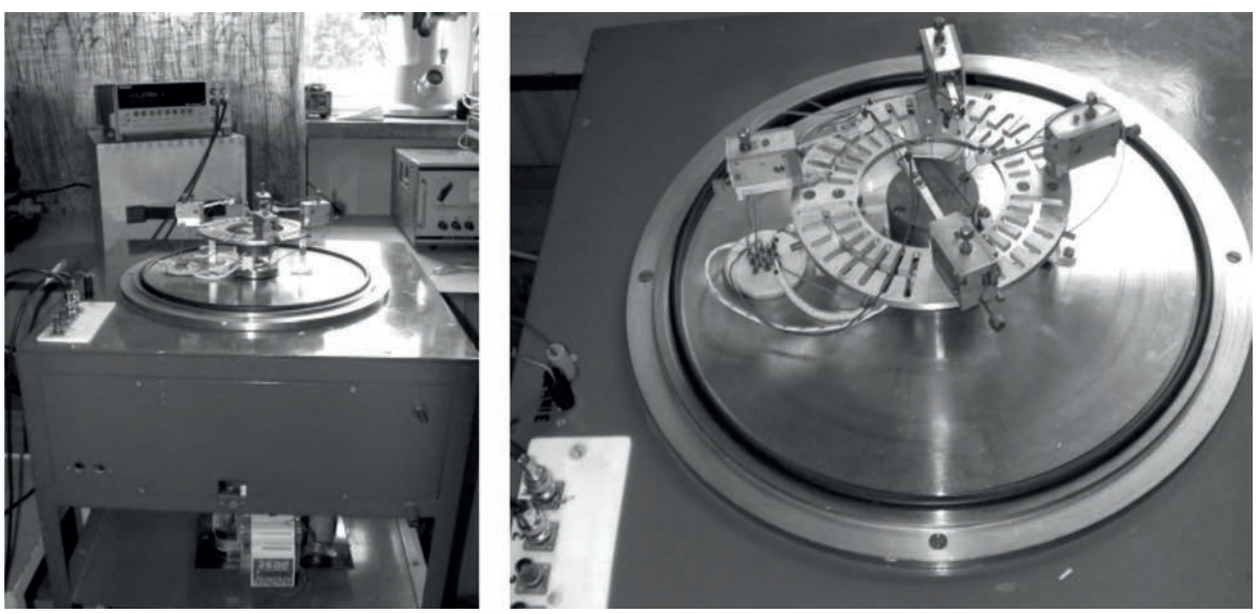

Rys. 7. Stanowisko do pomiarów narażeń prądowo-temperaturowych
Fig. 7. Laboratory stand for current-high temperature exposure measurements.

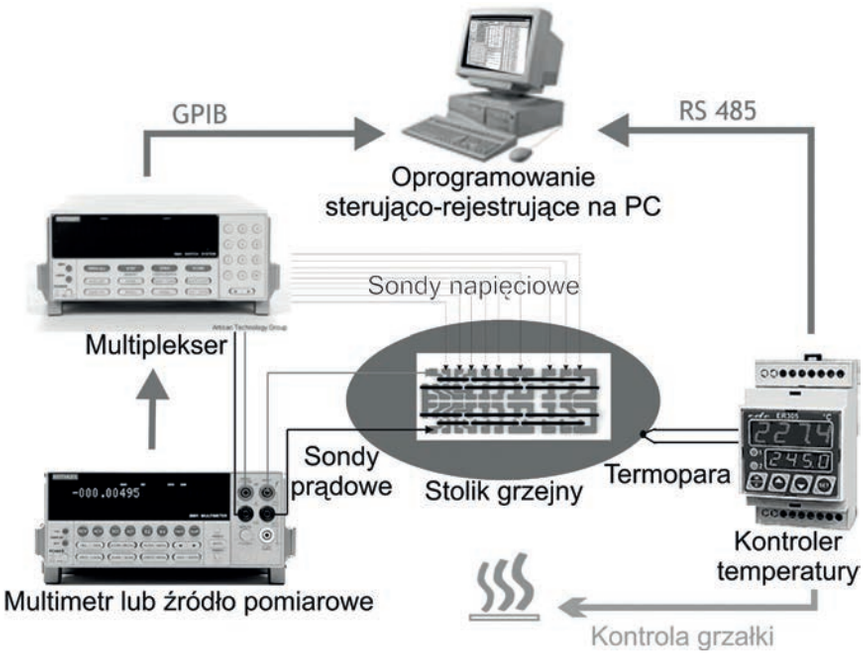

Rys. 8. Schemat stanowiska do pomiaru rezystancji podczas narażeń czasowo-temperaturowych.
Fig. 8. Diagram of a measuring stand used for thermal and current aging.

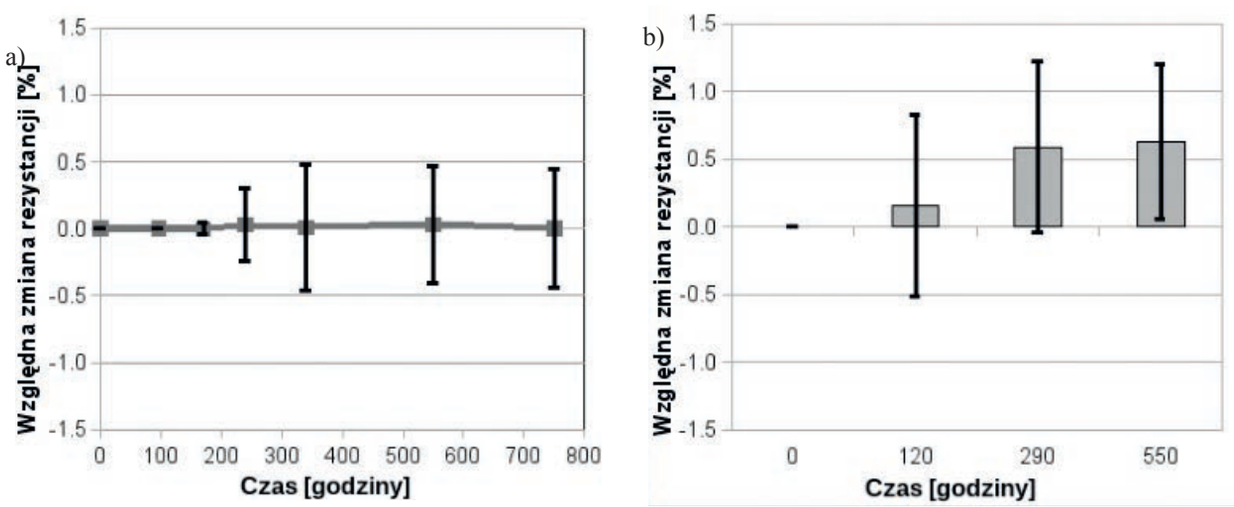

Rys. 9. Względne zmiany rezystancji rezystorów: a) R-100 Pbf narażonych na P = 1,6 W/mm^2, T = 80°C, b) R 10k Pbf narażonych na P = 1,6 W/mm^2, T = 80°C.
Fig. 9. Relative changes of resistance: a) R-100 Pbf exposed to P = 1.6 W/mm^2, T = 80°C, b) R-10k Pbf exposed to P = 1.6 W/mm^2, T = 80°C.

odczytane z urządzenia pomiarowego Keithley 2001 lub Keithley 2400. Z użyciem programu jest możliwe:

- wyznaczenie przebiegu profilu temperaturowego,
- wyznaczenie charakterystyki rezystancji w funkcji temperatury,
- zmierzenie rodziny charakterystyk U/I , R/I, R/U dla różnych temperatur (Keithley 2400),
- zrealizowanie cykli temperaturowych z ciągłą kontrolą parametrów elektrycznych.

Schemat stanowiska pomiarowego zaprezentowano na Rys. 8.

3.2. Pomiary stabilności termiczno-prądowej

Celem pomiarów było wyznaczenie dopuszczalnych warunków eksploatacji opracowanych rezystorów bezołowiowych oraz oszacowanie zmian rezystancji, wywołanych narażeniem na temperaturę i/lub przepływ prądu. Podana temperatura narażenia odnosi się do nastawy stolika grzejnego, zatem temperatura rezystora bez narażenia prądowego jest niższa niż nastawa, natomiast przy narażeniu prądowym może być ona wyższa. Zakładając przewodność cieplną podłoża alundowego równą 25 W/mK, szacowany przyrost temperatury rezystora względem powierzchni styku ze stolikiem wyniesie 25 K na każdy W/mm^2 wydzielonej mocy grzejnej.

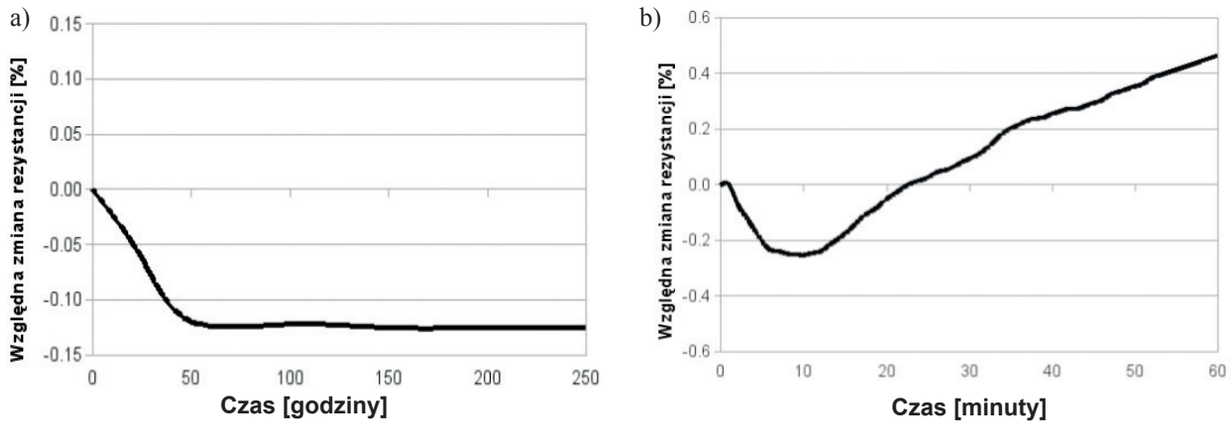

Rys. 10. Względne zmiany rezystancji rezystorów R-100 Pbf narażonych na: a) P = 1 W/mm^2 i 300°C, b) P = 4 W/mm^2 i 450°C.
Fig. 10. Relative changes of resistance of R-100 Pbf resistors exposed to: a) P = 1 W/mm^2 and 300°C, b) P = 4 W/mm^2 and 450°C.

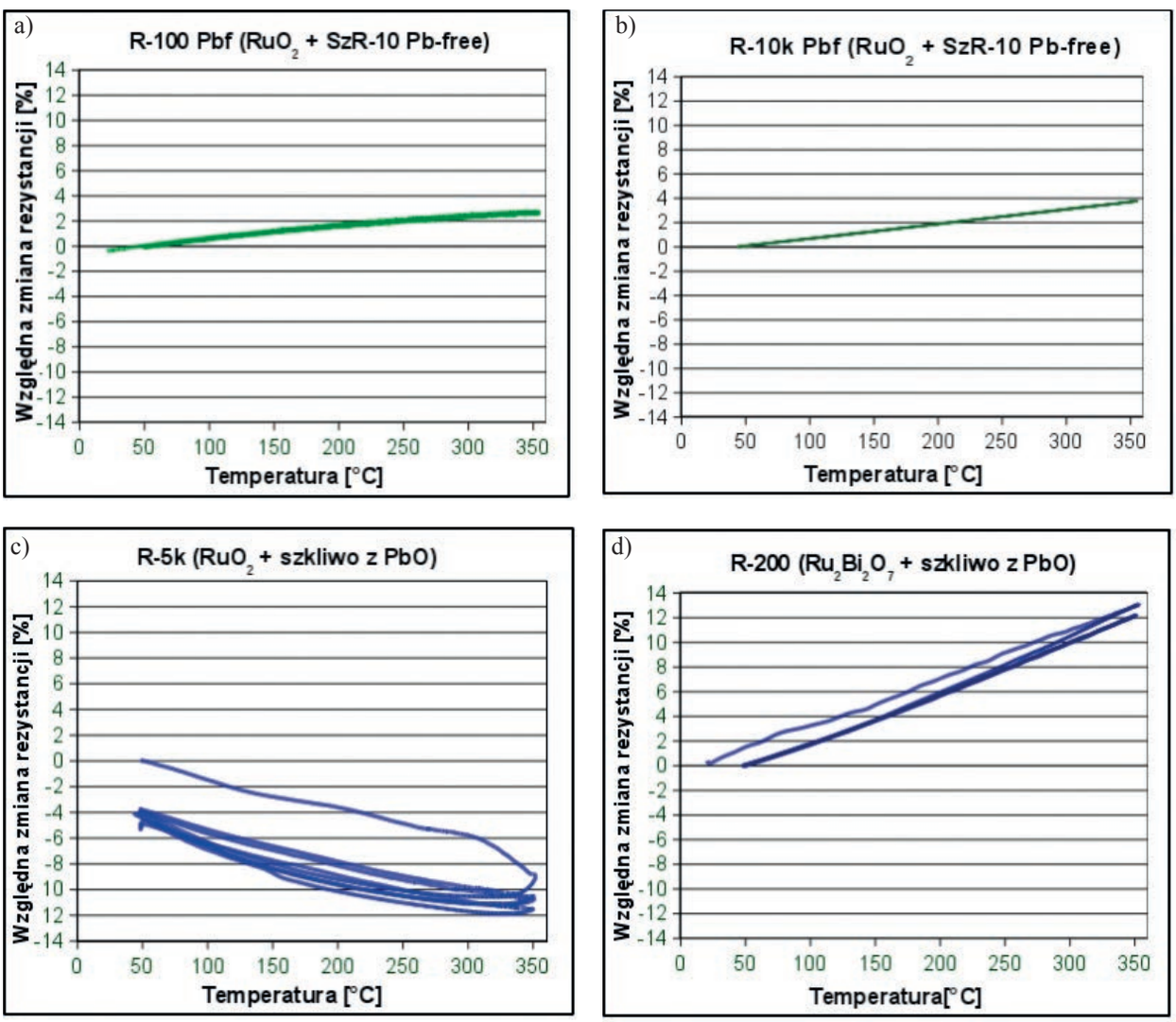

Rys. 11. Zależność rezystancji od temperatury dla kilku cykli pomiarowych 50 – 350°C dla rezystorów: a) bezołowiowego R-100 Pbf, b) bezołowiowego R-10k Pbf, c) R-5k RuO_2 i szkliwo tradycyjne, d) R-200, $Ru_2Bi_2O_7$ i szkliwo tradycyjne.
Fig. 11. Temperature-resistance dependence for a number of measuring cycles in temperatures 50 - 350°C for resistors: a) lead-free R-100 Pbf, b) lead-free R-10k Pbf, c) R 5k RuO_2 and traditional glass, d) of R-200, $Ru_2Bi_2O_7$ and traditional glass.

W pierwszym eksperymencie rezystory bezołowiowe z past „R-100 Pbf" i „R-10k Pbf" narażono prądowo wydzialając gęstość mocy 1,6 W/mm2 przy temperaturze stolika grzejnego 80°C. Pomiary każdego z 36 rezystorów były dokonywane po wychłodzeniu próbki do temperatury pokojowej. Obliczono średnią procentową zmianę rezystancji względem wartości początkowej oraz odchylenie standardowe zmiany rezystancji. W początkowym okresie eksploatacji od 50 do 200 godzin zwiększa się zakres zmienności rezystancji. Jest to najprawdopodobniej spowodowane relaksacją naprężeń cieplnych pomiędzy warstwą przewodzącą i rezystywną. Następnie dochodzi do stabilizacji wartości rezystancji, Rys. 9a - b.

W drugim eksperymencie narażeniom prądowo-napięciowym poddano rezystory wykonane z pasty bezołowiowej „R-100 Pbf". Wartość rezystancji była mierzona podczas narażenia (*in-situ*). Pomiar obejmował sumaryczną rezystancję 36 połączonych szeregowo rezystorów. Podczas pracy w temperaturze stolika grzejnego 300°C, przy gęstości mocy 1 W/mm^2, po początkowej niewielkiej zmianie rezystancji w ciągu pierwszych 50 godzin co zostało uwidocznione na Rys. 10a, następuje stabilizacja rezystancji. Dopiero podniesienie temperatury stolika grzejnego do 450°C w połączeniu z narażeniem gęstością mocy 4 W/mm^2 powoduje postępującą degradację rezystora, zgodnie z wykresem zamieszczonym na Rys. 10b. Szybkość degradacji, która w tych warunkach postępuje w sposób przewidywalny, wynosi około 1% na godzinę. Jest więc dopuszczalna krótkotrwała eksploatacja rezystorów w tych warunkach.

3.3. Pomiary odporności na cykliczne narażenia termiczne

W trzecim eksperymencie wykonano pomiary porównawcze rezystancji w funkcji temperatury dla trzech cykli temperaturowych w zakresie od 50 do 350°C, przy zaniedbywanym narażeniu prądowym (poniżej 1 mW/mm^2) wywołanym jedynie prądem pomiarowym. Wartość rezystancji byłą mierzona podczas narażenia (*in-situ*). Pomiar obejmował sumaryczną rezystancję 36 połączonych szeregowo rezystorów. Pomiary wykonano dla rezystorów z czterech past rezystywnych: „R-100 Pbf" ze szkliwem bezołowiowym „SzR-10" (Rys. 11a), „R-10k Pbf" ze szkliwem bezołowiowym „SzR-16 Pbf" (Rys. 11b) „R-200" ze szkliwem ołowiowo-boro-krzemowym (Rys. 11c) oraz „R-5k" z fazą przewodzącą $Bi_2Ru_2O_7$ i szkliwem ołowiowo-boro-krzemowym (Rys. 11d). Całkowity czas trwania pojedynczego cyklu wynosił 2400 sekund, w tym 500 sekund przypadało na grzanie. Pomiary wykazały, że każde kolejne narażenie rezystorów ze szkliwami zawierającymi PbO prowadzi do przemieszczania się charakterystyki rezystancji w funkcji temperatury o -4% w przypadku rezystorów z pasty „R-5k" i +2% w przypadku rezystorów z pasty „R-200". To przemieszczenie jest oznaką niestabilności tych warstw, co zostało pokazane na Rys. 11c - d. Natomiast w przypadku rezystorów z RuO_2 ze szkliwem bezołowiowym „SzR-10" i „SzR-16 (Rys. 11a - b) przy każdym kolejnym narażeniu rezystorów, położenie charakterystyki się nie zmieniło. Dowodzi to stabilności tych warstw i odporności na temperaturę pracy do 350°C.

4. Wnioski

W pracy przedstawiono rezystory wykonane z nowatorskich i ekologicznych past rezystywnych, które posiadają one dwie istotne zalety w stosunku do past tradycyjnych. Po pierwsze, spełniają one wymagania dyrektywy RoHS, co umożliwia ich stosowanie w wyrobach konsumenckich przeznaczonych na rynek europejski. Po drugie, z uwagi na zastosowanie stabilnej fazy przewodzącej RuO_2 oraz szkliwa bezołowiowego o temperaturach mięknięcia wyższych niż typowe szkliwa ołowiowo-boro-krzemowe, rezystory wykonane z tych past wykazują znaczącą odporność na pracę w wysokich temperaturach i przy znacznym narażeniu na wydzielaną moc. W rodzącej się elektronice wysokotemperaturowej, w której elementami aktywnymi są struktury oparte na węgliku krzemu, szerokie zastosowania mają podłoża ceramiczne i techniki montażu drutowego oraz klejenie, czyli połączenia umożliwiające eksploatację układu elektronicznego w temperaturach do 300°C. Istnieje znaczące zapotrzebowanie na stabilne termicznie elementy bierne pracujące w tym zakresie temperatur. A więc opracowane rezystory bezołowiowe spełniają takie wymogi.

Literatura

[1] Rane S., Prudenziati M., Mortena B.: Environment friendly perovskite ruthenate based thick film resistors, *Materials Letters*, 2007, 61, 2, 595 - 99

[2] Cheng Y., Xiao H., Guo W., Guo W.: Structure and crystallization kinetics of $PbO–B_2O_3$ glasses, *Ceramics International*, 2007, 33, 7, 1341 - 47

[3] Morten B., Masoero A., Prudenziati M., Manfredini T.: Evolution of ruthenate-based thick film cermet resistors: *J. Phys. D: Appl. Phys.*, 1994, 27, 10, 2227 - 35

[4] Pike G. E., Seager C. H.: Electrical properties and conduction mechanism of Ru-based thick-film (cermet) resistors, *J. AppL Phys.*, 1977, 48, 5152 - 69

[5] Kuiel R., Broukal J., Kindl D.: X-Ray and microscopic investigations of resistors containing CdO and RuO_2, *IEEE Transacilons on Components, Hybrids and Manufacturing Technology*", 1981, 4, 3, 245 - 49

[6] Beyerlein R. A., Horowitz H. S., Longo J. M.: The electrical properties of $A_2[Ru_{2-x}A_x]O_{7-y}$ (A = Pb or

Bi) pyrochlores as a function of composition and temperature, *Journal of Solid State Chemistry*, 1988, 72, 1, 2 - 13

[7] Młożniak A., Jakubowska M., Kiełbasiński K., Zwierkowska E.: Nowa generacja past rezystywnych nie zawierających ołowiu i kadmu spełniających dyrektywę RoHS, *Materiały Elektroniczne*, 2006, 34 , 3, 5 - 18

[8] Kiełbasiński K., Młożniak A., Jakubowska M.: Environmental friendly thick film resistors with wide resistance range, *Materiały Elektroniczne,* 2008, 36, 4, 39 - 46

[9] Pflieger R., Lefebvre L., Malki M., Allix M., Grandjean A.: Behaviour of ruthenium dioxide particles in borosilicate glasses and melts, *Journal of Nuclear Materials*, 2009, 389 , 450 - 457

[10] Kiełbasiński K., Zwierkowska E., Achmatowicz S., Młożniak A., Jakubowska M.: Badanie właściwości szkliw pod kątem zastosowań w grubowarstwowych mikrorezystorach fotoformowalnych, *Materiały Elektroniczne*, 2013, 41, 1, pp. 10 - 16

STRESZCZENIA WYBRANYCH ARTYKUŁÓW PRACOWNIKÓW ITME

Polyelectrolyte multilayer film modification for chemo-mechano-regulation of endothelial cell response

Mzyk A.[1], Lackner J. M.[2], Wilczek P.[3], Lipińska L.[4], Niemiec-Cyganek A.[3], Samotus A.[3], Morenc M.[3]

[1] Institute of Metallurgy and Materials Science, Polish Academy of Sciences, 25 Reymonta Street, 30-059 Krakow, Poland

[2] Joanneum Research Forschungsges mbH, Institute of Surface Technologies and Photonics, Functional Surfaces, Leobner Strasse 94, A-8712 Niklasdorf, Austria

[3] Foundation for Cardiac Surgery Development, Wolnosci Street 345a, 41-800 Zabrze, Poland

[4] Institute of Electronic Materials Technology, Wolczynska 133, 01-919 Warsow, Poland

RSC Advances, 2016, 6, 11, 8811 - 8828

The new multilayer polyelectrolyte films (PEMs) that are able to simulate the structure and functions of the extracellular matrix have become a powerful tool for tailoring biointerfaces of implants. In this study, bioactive PEM coatings have been investigated as a supportive system for efficient endothelialization of cardiovascular implants. The modern films were designed in a manner that allows one to potentially induce specific response from the tissues surrounding the biomaterial due to its chemical composition as well as mechanical properties. The PEM rigidity was regulated by the cross-linking chemistry as well as nanoparticle incorporation, while biochemical modification was performed by the VEGF adsorption within coatings. Obtained results have shown that PEM/VEGF films enhanced in vitro spreading and proliferation of endothelial cells, whereas VEGF presence inhibited IL-6 production and release. Since non-functionalized films also contributed to proliferation of endothelial cells and cytokine secretion, it may be supposed that PEM stiffness acts in synergy with the growth factor, but probably through a different pathway. Results clearly demonstrate the effectiveness of the proposed endothelialization strategy and confirm correlation between the chemical and mechanical properties of the PEMs in vitro.

'Clickable' ZnO nanocrystals: the superiority of a novel organometallic approach over the inorganic sol–gel procedure

Grala A.[1,2], Wolska-Pietkiewicz M.[1], Danowski W.[1], Wróbel Z.[2], Grzonka J.[2,3,4], Lewiński J.[1,2]

[1] Warsaw University of Technology, Faculty of Chemistry, Noakowskiego 3, 00-664 Warsaw, Poland

[2] Polish Academy of Sciences, Institute of Physical Chemistry, Kasprzaka 44/52, 01-224 Warsaw, Poland

[3] Warsaw University of Technology, Faculty of Materials Science and Engineering, Wołoska 141, 02-507 Warsaw, Poland

[4] Institute of Electronic Materials Technology, Wolczynska 133, 01-919 Warsaw, Poland

Chemical Communications, 2016,52, 7340 - 7343

We demonstrate for the first time a highly efficient Cu(I)-catalyzed alkyne–azide cycloaddition reaction on the surface of ZnO nanocrystals with retention of their photoluminescence properties. Our comparative studies highlight the superiority of a novel self-supporting organometallic method for the preparation of brightly luminescent and well-passivated ZnO nanocrystals over the traditional sol–gel procedure.

Large-area high-quality graphene on Ge(001)/Si(001) substrates

Pasternak I.[1], Dabrowski P.[2], Ciepielewski P.[1], Kolkovsky V.[3], Klusek Z.[2], Baranowski J. M.[1], Strupinski W.[1]

[1] Institute of Electronic Materials Technology, Wolczynska 133, 01-919 Warsaw, Poland

[2] Department of Solid States Physics, University of Lodz, Pomorska 149/153, Lodz, Poland

[3] Institute of Physics, Polish Academy of Sciences, Al. Lotnikow 32/46, Warsaw, 02-668 Poland

Nanoscale, 2016, 8, 11241 - 11247

Various experimental data revealing large-area high-quality graphene films grown by the CVD method on Ge(001)/Si(001) substrates are presented. SEM images have shown that the structure of nano-facets is formed on the entire surface of Ge(001), which is covered by a graphene layer over the whole macroscopic sample surface of 1 cm^2. The hill-and-valley structures are positioned 90° to each other and run along the <100> direction. The hill height in relation to the valley measured by STM is about 10 nm. Raman measurements have shown that a uniform graphene monolayer covers the nano-facet structures on the Ge(001) surface. Raman spectroscopy has also proved that the grown graphene monolayer is characterized by small strain variations and minimal charge fluctuations. Atomically resolved STM images on the hills of the nanostructures on the Ge(001) surface have confirmed the presence of a graphene monolayer. In addition, the STS/CITS maps show that high-quality graphene has been obtained on such terraces. The subsequent coalescence of graphene domains has led to a relatively well-oriented large-area layer. This is confirmed by LEED measurements, which have indicated that two orientations are preferable in the grown large-area graphene monolayer. The presence of large-area coverage by graphene has been also confirmed by low temperature Hall

measurements of a macroscopic sample, showing an n-type concentration of 9.3×10^{12} cm^{-2} and a mobility of 2500 cm^2 V^{-1} s^{-1}. These important characteristic features of graphene indicate a high homogeneity of the layer grown on the large area Ge(001)/Si(001) substrates.

Optical-quality controllable wet-chemical doping of graphene through a uniform, transparent and low-roughness F4-TCNQ/MEK layer

Misseeuw L.[1], Krajewska A.[2,3], Pasternak I.[3], Ciuk T.[3], Strupinski W.[3], Reekmans G.[4], Adriaensens P.[4], Geldof D.[5], Blockhuys F.[5], Van Vlierberghe S.[1,5,6], Thienpont H.[1], Dubruel P.[6], Vermeulen N.[1]

[1] Brussels Photonics Team (B-PHOT), Dept. of Applied Physics and Photonics (IR-TONA), Vrije Universiteit Brussel, Pleinlaan 2, B-1050 Brussels, Belgium

[2] Institute of Optoelectronics, Military University of Technology, Gen. S. Kaliskiego 2, 00-908 Warsaw, Poland

[3] Institute of Electronic Materials Technology, Wolczynska 133, 01-919 Warsaw, Poland

[4] Applied and Analytical Chemistry, Institute for Materials Research (IMO), Hasselt University, Agoralaan 1-Building D, B-3590 Diepenbeek, Belgium

[5] Department of Chemistry, University of Antwerp, Groenborgerlaan 171, B-2020 Antwerp, Belgium

[6] Polymer Chemistry & Biomaterials Research Group, Ghent University, Krijgslaan 281 (S4 Bis), B-9000 Ghent, Belgium

RSC Advances, 2016, 6, 104491 - 104501

Controllable chemical doping of graphene has already proven very useful for electronic applications, but when turning to optical and photonic applications, the additional requirement of having both a high transparency and a low surface roughness has, to our knowledge, not yet been fulfilled by any chemical dopant system reported so far. In this work, a new method that meets for the first time this optical-quality requirement while also providing efficient, controllable doping is presented. The method relies on F4-TCNQ dissolved in methyl ethyl ketone (MEK) yielding a uniform deposition after spin coating because of an extraordinary charge transfer interaction between the F4-TCNQ and MEK molecules. The formed F4-TCNQ/MEK layer exhibits a very high surface quality and optical transparency over the visible-infrared wavelength range between 550 and 1900 nm. By varying the dopant concentration of F4-TCNQ from 2.5 to 40 mg ml^{-1} MEK, the doping effect can be controlled between $\Delta n = +5.73 \times 10^{12}$ cm^{-2} and $+1.09 \times 10^{13}$ cm^{-2} for initially strongly p-type hydrogen-intercalated graphene grown on 6H-silicon-carbide substrates, and between Δn = +5.56 × 1012 cm−2 and $+1.04 \times 10^{13}$ cm^{-2} for initially weakly p-type graphene transferred on silicon samples. This is the first time that truly optical-quality chemical doping of graphene is demonstrated, and the obtained doping values exceed those reported before for F4-TCNQ-based graphene doping by as much as 50%.

Printed HF antennas for RFID on-metal transponders

Janeczek K.[1], Arazna A.[1], Salski B.[2], Lipiec K.[1], Jakubowska M.[3,4]

[1] Tele and Radio Research Institute, Warsaw, Poland

[2] Institute of Radioelectronics, Warsaw University of Technology, Warsaw, Poland

[3] Institute of Electronic Materials Technology, Warsaw, Poland

[4] Institute of Metrology and Biomedical Engineering, Warsaw University of Technology, Warsaw, Poland

Circuit World, 2016, 42, 1, pp.2

Purpose - The purpose of this paper is to investigate screen-printed high-frequency (HF) antennas for radio frequency identification (RFID) on-metal transponders in which a magnetic sheet was used as a substrate material.

Design/methodology/approach - A transponder antenna was designed in the form of square coil using a high-frequency electromagnetic software. Then, the antenna was fabricated with screen printing technique on two different magnetic sheets (RFN4 and RFN7) and on polyethylene naphthalate (PEN) foil for comparison. Its printing was carried out with polymer pastes based on silver flakes (PM-406 and SF). Thickness, track width and spacing were examined for the antennas using digital microscope and contact profilometer. Resistance and inductance were also measured, and resonant frequency, quality factor and target values of capacitance to achieve resonant frequency of the tested antenna at 13.56 MHz were calculated. Finally, RFID chips were mounted to the prepared antennas using an isotropic conductive adhesive, and a maximum read distance was measured with a reader installed in a smartphone.

Findings - It was found that an antenna thickness on the magnetic sheets used was higher than on PEN foil. At the same time, surface roughness of the fabricated antennas on these sheets was revealed to be higher as well. Inductance of the measured antennas exhibited good conformity with the antenna design, but higher divergence was noticed in the measured resistance. Its lowest value was achieved when the antenna was printed with the paste PM-406 on PEN foil and the highest one when it was fabricated with the paste SF on the same substrate. This suggests that high attention needs to be paid to a polymer paste selected for antenna printing. The performed tests showed that the magnetic sheet RFN4 seems to be better substrate for on-metal transponders compared to RFN7 due to lower resistance and higher quality factor of the prepared antennas.

Research limitations/implications - Further investigations are required to examine mechanical and thermal durability of the HF antennas printed on the magnetic sheets.

Practical implications - The investigated HF antennas fabricated on magnetic sheets can find application in near field communication (NFC) transponders designed to be placed on metallic surfaces, e.g. on frames of advertising screens.

Originality/value - Influence of used magnetic sheets and

polymer pastes on geometry and electrical properties of HF antennas for RFID on-metal transponders was investigated. The presented investigations can be interesting for NFC/RFID designers who are involved in designing systems suitable for metallic surfaces

Ambient Temperature Growth of Mono- and Polycrystalline NbN Nanofilms and Their Surface and Composition Analysis

Krause S.[1], Afanas'ev V.[2], Desmaris V.[1], Meledin D.[1], Pavolotsky A.[1], Belitsky V.[1], Lubenschenko A.[2], Batrakov A.[2], Rudzinski M.[3], Pippel E.[4]

[1] Group for Advanced Receiver Development, Chalmers University of Technology, Gothenburg, Sweden

[2] Department of General Physics and Nuclear Fusion, National Research University "Moscow Power Engineering Institute", Moscow, Russia

[3] Institute of Electronic Materials Technology (ITME), Warsaw, Poland

[4] Max Planck Institute of Microstructure Physics, Halle, Germany

This paper presents the studies of high-quality 5-nm-thin NbN films deposited by means of reactive dc magnetron sputtering at room temperature. The deposition without substrate heating offers major advantages from a processing point of view and motivates the extensive composition and surface characterization and comparison of the present films with high-quality films grown at elevated temperatures. Monocrystalline NbN films have been epitaxially grown onto hexagonal GaN buffer layers (0002) and show a distinct low defect interface as confirmed by high-resolution TEM. The critical temperature T_c of the films on the GaN buffer layer reached 10.4 K. Furthermore, a polycrystalline structure was observed on films grown onto Si (100) substrates, exhibiting a T_c of 8.1 K, albeit a narrow transition from the normal to the superconducting state. X-ray photoelectron spectroscopy and reflected electron energy loss spectroscopy verified that the composition of NbN was identical irrespective of applied substrate heating. Moreover, the native oxide layer at the surface of NbN has been identified as NbO_2 and, thus, is in contrast to the Nb_2O_5, usually claimed to be formed at the surface of Nb when exposed to air. These findings are of significance since it was proven the possibility of growing epitaxial NbN onto GaN buffer layer in the absence of high temperatures, hence paving the way to employ NbN in more advanced fabrication processes involving a higher degree of complexity. The eased integration and employment of liftoff techniques could, in particular, lead to improved performance of cryogenic ultrasensitive terahertz electronics.

g-factors of conduction electrons and holes in Bi_2Se_3 three-dimensional topological insulator

Wolos A.[1,2], Szyszko S.[2], Drabinska A.[2], Kaminska M.[2], Strzelecka S. G.[3], Hruban A.[3], Materna A.[3], Piersa M.[3], Borysiuk J.[1,2], Sobczak K.[1], Konczykowski M.[4]

[1] Institute of Physics, Polish Academy of Sciences, Al. Lotnikow 32/46, 02-668 Warsaw, Poland

[2] Faculty of Physics, University of Warsaw, ul. Pasteura 5, 00-681 Warsaw, Poland

[3] Institute of Electronic Materials Technology, ul. Wolczynska 133, 01-919 Warsaw, Poland

[4] Laboratoire des Solides Irradiés, CNRS-UMR 7642 and CEA-DSM-IRAMIS, Ecole Polytechnique, F-91128 Palaiseau Cedex, France

Physical Review B, 2016, 93, 155114

Bulk-related conduction electron spin resonance and conduction hole spin resonance were investigated in Bi_2Se_3, a three-dimensional topological insulator. Electrons in the conduction band and holes in the valence band both have spin ½. The effective g-factors for conduction electrons are equal to 27.3 ± 0.15 for magnetic field parallel to the c axis and 19.48 ± 0.07 for magnetic field perpendicular to the c axis, whereas for conduction holes 29.90 ± 0.09 for magnetic field parallel and 18.96 ± 0.04 for magnetic field perpendicular to the c axis, respectively. Nonparabolicity effects were not observed in the investigated low carrier concentration range, below $8 \times 10^{17}cm^{-3}$. Large g-factors, higher by an order of magnitude than the free electron value, are due to strong spin-orbit interactions in Bi_2Se_3. The striking similarity of the spin resonances due to conduction electrons and holes confirms the peculiar symmetry between the conduction and valence bands of Bi_2Se_3, both having similar effective masses and spin character.

Manipulating the Topological Interface by Molecular Adsorbates: Adsorption of Co--Phthalocyanine on Bi_2Se_3

Caputo M.[1,2], Panighel M.[3,2], Lisi S.[4,5], Khalil L.[1,6], Di Santo G.[2], Papalazarou E.[1], Hruban A.[7], Konczykowski M.[8] et al.

[1] Laboratoire de Physique des Solides, CNRS, Universitè Paris-Sud, Université Paris-Saclay, 91405 Orsay Cedex, France

[2] Laboratory Micro & Nano-Carbon, Elettra - Sincrotrone Trieste S.C.p.A., s.s.14 Km 163.5, 34149 Trieste, Italy

[3] Catalan Institute of Nanoscience and Nanotechnology (ICN2), CSIC and The Barcelona Institute of Science and Technology, Campus UAB, Bellaterra, 08193 Barcelona,Spain

[4] Dipartimento di Fisica, Università di Roma La Sapienza, Piazzale A. Moro 5, 00185 Roma, Italy

[5] Institut Néel, CNRS/UGA UPR2940, 25 Rue des Martyrs BP 166, 38042 Grenoble, France

[6] Synchrotron SOLEIL, L'Orme des Merisiers, Saint-Aubin, BP48, 91192 Gif-sur-Yvette Cedex, France

[7] Institute of Electronic Materials Technology, 01-919 Warsaw, Poland

[8] Laboratoire des Solides Irradiés, Ecole Polytechnique, CNRS, CEA, Université Paris-Saclay, 91128 Palaiseau Cedex, France

Nano Letters, 2016, 16, 6, 3409 - 3414

Topological insulators are a promising class of materials for applications in the field of spintronics. New perspectives in this field can arise from interfacing metal–organic molecules with the topological insulator spin-momentum locked surface states, which can be perturbed enhancing or suppressing spintronics-relevant properties such as spin coherence. Here we show results from an angle-resolved photemission spectroscopy (ARPES) and scanning tunnelling microscopy (STM) study of the prototypical cobalt phthalocyanine (CoPc)/Bi_2Se_3 interface. We demonstrate that that the hybrid interface can act on the topological protection of the surface and bury the Dirac cone below the first quintuple layer.

Comparative study of radiation-induced damage in magnesium aluminate spinel by means of IL, CL and RBS/C techniques

Jozwik I.[1], Jagielski J.[1,2], Gawlik G.[1], Jozwik P.[1], Ratajczak R.[2], Panczer G.[3], Moncoffre N.[4], Wajler A.[1], Sidorowicz A.[1], Thome L.[5]

[1] Institute of Electronic Materials TechnologyWarsawPoland

[2] National Centre for Nuclear ResearchOtwock, SwierkPoland

[3] Institut Lumière Matière, UMR5306 Université Lyon 1-CNRSUniversité de LyonVilleurbanne CedexFrance

[4] Institute de Physique Nucléaire Lyon, UMR5822Villeurbanne CedexFrance

[5] Centre de Spectrométrie Nucléaire et de Spectrométrie de Masse, IN2P3-CNRSUniversité Paris-SudOrsay CedexFrance

Physics and Chemistry of Minerals, 2016, 43, 6, 439 - 445

A comparative study of damage accumulation in magnesium aluminate spinel ($MgAl_2O_4$) has been conducted using ionoluminescence (IL), cathodoluminescence (CL) and Rutherford Backscattering Spectrometry/channeling (RBS/C) techniques. $MgAl_2O_4$ single crystal and polycrystalline samples were irradiated with 320 keV Ar^+ ions at fluencies ranging from 1×10^{12} to 2×10^{16} cm^{-2} in order to create various levels of radiation damage. RBS/C measurements provided quantitative data about damage concentration in the samples. These values were then compared to the luminescence measurements. The results obtained by IL and RBS/C methods demonstrate a two-step character of damage buildup process. The CL data analysis points to the three-step damage accumulation mechanism involving the first defect transformation at fluencies of about 10^{13} cm^{-2} and second at about 10^{15} cm^{-2}. The rate of changes resulting from the formation of nonluminescent recombination centers is clearly nonlinear and cannot be described in terms of continuous accumulation of point defects. Both, IL and CL techniques, appear as new, complementary tools bringing new possibilities in the damage accumulation studies in single- and polycrystalline materials.

Surface and interface structure of quasi-free standing graphene on SiC

Melios C.[1,2], Spencer S.[1], Shard A.[1], Strupiński W.[3], Silva S. R. P.[2], Kazakova O.[1]

[1] National Physical Laboratory, Teddington, TW11 0LW, UK

[2] Advanced Technology Institute, University of Surrey, Guildford, Surrey, GU2 7XH, UK

[3] Institute of Electronic Materials Technology, Wólczyńska 133, 01-919 Warsaw, Poland

2D Materials, 2016, 3, 2, 025023

We perform local nanoscale studies of the surface and interface structure of hydrogen intercalated graphene on 4H–SiC(1000). In particular, we show that intercalation of the interfacial layer results in the formation of quasi-free standing one layer graphene (QFS 1LG) with change in the carrier type from n- to p-type, accompanied by a more than four times increase in carrier mobility. We demonstrate that surface enhanced Raman scattering (SERS) reveals the enhanced Raman signal of Si–H stretching mode, which is the direct proof of successful intercalation. Furthermore, the appearance of D, D + D' as well as C–H peaks for the quasi-free standing two layer graphene (QFS 2LG) suggests that hydrogen also penetrates in between the graphene layers to locally form C–H sp^3 defects that decrease the mobility. Thus, SERS provides a quick and reliable technique to investigate the interface structure of graphene which is in general not accessible by other conventional methods. Our findings are further confirmed by Kelvin probe force microscopy and x-ray photoelectron spectroscopy.

Low-noise epitaxial graphene on SiC Hall effect element for commercial applications

Ciuk T.[1,2], Petruk O.[3], Kowalik A.[1], Jozwik I.[1], Rychter A.[4], Szmidt J.[2], Strupinski W.[1]

[1] Institute of Electronic Materials Technology, Wolczynska 133, 01-919 Warsaw, Poland

[2] Institute of Microelectronics and Optoelectronics, Warsaw University of Technology, Koszykowa 75, 00-662 Warsaw, Poland

[3] Industrial Research Institute for Automation and Measurements PIAP, Al. Jerozolimskie 202, 02-486 Warsaw, Poland

[4] Institute of Radioelectronics and Multimedia Technology, Warsaw University of Technology, Koszykowa 75, 00-662 Warsaw, Poland

Applied Physics Letters, 2016, 108, 223504

In this report, we demonstrate a complete Hall effect element that is based on quasi-free-standing monolayer graphene synthesized on a semi-insulating on-axis Si-terminated 6H-SiC substrate in an epitaxial Chemical Vapor Deposition process. The device offers the current-mode sensitivity of 87 V/AT and low excess noise (Hooge's parameter $\alpha_H < 2 \times 10^{-3}$) enabling

room-temperature magnetic resolution of 650 nT/Hz$^{0.5}$ at 10 Hz, 95 nT/Hz$^{0.5}$ at 1 kHz, and 14 nT/Hz$^{0.5}$ at 100 kHz at the total active area of 0.1275 mm^2. The element is passivated with a silicone encapsulant to ensure its electrical stability and environmental resistance. Its processing cycle is suitable for large-scale commercial production and it is available in large quantities through a single growth run on an up to 4-in SiC wafer.

Strong interband Faraday rotation in 3D topological insulator Bi_2Se_3

Ohnoutek L.[1], Hakl M.[2], Veis M.[1], Piot B. A.[2], Faugeras C.[2], Martinez G.[2], Yakushev M. V.[3,4], Martin R. W.[3], Drasar C.[5], Materna A.[6], Strzelecka G.[6], Hruban A.[6], Potemski M.[2], Orlita M.[1,2]

[1] Institute of Physics, Charles University, Ke Karlovu 5, CZ-121 16 Praha 2, Czech Republic

[2] Laboratoire National des Champs Magnétiques Intenses, CNRS-UJF-UPS-INSA, 25, avenue des Martyrs, 38042 Grenoble, France

[3] Department of Physics, SUPA, Strathclyde University, G4 0NG Glasgow, UK

[4] Ural Federal University and Institute of Solid State Chemistry of RAS, Ekaterinburg, 620002, Russia

[5] Institute of Applied Physics and Mathematics, Faculty of Chemical Technology, University of Pardubice, Studentská 84, 532 10 Pardubice, Czech Republic

[6] Institute of Electronic Materials Technology, ul. Wolczynska 133, PL 01-919 Warsaw, Poland

Scientific Reports, 2016, 6, 19087

The Faraday effect is a representative magneto-optical phenomenon, resulting from the transfer of angular momentum between interacting light and matter in which time-reversal symmetry has been broken by an externally applied magnetic field. Here we report on the Faraday rotation induced in the prominent 3D topological insulator Bi_2Se_3 due to bulk interband excitations. The origin of this non-resonant effect, extraordinarily strong among other non-magnetic materials, is traced back to the specific Dirac-type Hamiltonian for Bi2Se3, which implies that electrons and holes in this material closely resemble relativistic particles with a non-zero rest mass.

Graphene FET Gigabit ON-OFF Keying Demodulator at 96 GHz

Habibpour O.[1], He Z. S.[1], Strupinski W.[2], Rorsman N.[1], Ciuk T.[2], Ciepielewski P.[2], Zirath H.[1]

[1] Chalmers, Microwave Elect. Lab., Dep. Microtechnol & Nanosci, S-41296 Gothenburg, Sweden

[2] Inst. Elect. Mat. Technol., 01-919 Warsaw, Poland

IEEE Electron Device Letters, 2016, 37, 3, 333 - 336

We demonstrate the demodulation of a multi-Gb/s ON-OFF keying (OOK) signal on a 96 GHz carrier by utilizing a 250-nm graphene field-effect transistor as a zero bias power detector. From the eye diagram, we can conclude that the devices can demodulate the OOK signals up to 4 Gb/s.

Numerical simulations of epitaxial growth in MOVPE reactor as a tool for aluminum nitride growth optimization

Skibinski, J.[1], Caban, P.[2], Wejrzanowski T.[1], Grybczuk M.[1], Kurzydlowski, K. J.[1]

[1] Warsaw Univ. Technol. Fac. Mat. Sci & Engn, Woloska 141, 02-507 Warsaw, Poland

[2] Inst. Elect. Mat. Technol., Wolczynska 133, 01-919 Warsaw, Poland

Journal of Power Technologies, 2016, 96, 2, 110 - 114

The present study concerns numerical simulations and experimental measurements on the influence of inlet gas mass flow rate on the growth rate of aluminum nitride crystals in Metalorganic Vapor Phase Epitaxy reactor model AIX-200/4RF-S. The aim of this study was to design the optimal process conditions for obtaining the most homogeneous product. Since there are many agents influencing reactions relating to crystal growth such as temperature, pressure, gas composition and reactor geometry, it is difficult to design an optimal process. Variations of process pressure and hydrogen mass flow rates have been considered. Since it is impossible to experimentally determine the exact distribution of heat and mass transfer inside the reactor during crystal growth, detailed 3D modeling has been used to gain insight into the process conditions. Numerical simulations increase the understanding of the epitaxial process by calculating heat and mass transfer distribution during the growth of aluminum nitride crystals. Including chemical reactions in the numerical model enables the growth rate of the substrate to be calculated. The present approach has been applied to optimize homogeneity of AlN film thickness and its growth rate.

Direct comparison of shot-to-shot noise performance of all normal dispersion and anomalous dispersion supercontinuum pumped with sub--picosecond pulse fiber-based laser

Klimczak M.[1], Sobon G.[2], Kasztelanic R.[1], Abramski K. M.[2], Buczynski R.[1,3]

[1] Inst. Elect. Mat. Technol., Glass Dept., Wolczynska 133, 01-919 Warsaw, Poland

[2] Wroclaw. Univ. Technol., Laser & Fiber Elect. Grp., Wybrzeze Wyspianskiego 27, 50-370 Wroclaw, Poland

[3] Univ. Warsaw., Fac. Phys., Pasteura 7, 02-093 Warsaw, Poland

Scientific Reports, 2016, 6, 19284

Coherence of supercontinuum sources is critical for applications involving characterization of ultrafast or rarely occurring phenomena. With the demonstrated spectral coverage of supercontinuum extending from near-infrared to over 10 μm in a single nonlinear fiber, there has been a clear push for the bandwidth rather than for attempting to optimize the dynamic properties of the generated spectrum. In this work we provide an experimental assessment of the shot-to-shot noise performance of supercontinuum generation in two types of soft glass photonic crystal fibers. Phase coherence and intensity fluctuations are compared for the cases of an anomalous dispersion-pumped fiber and an all-normal dispersion fiber. With the use of the dispersive Fourier transformation method, we demonstrate that a factor of 100 improvement in signal-to-noise ratio is achieved in the normal-dispersion over anomalous dispersion-pumped fiber for 390 fs long pump pulses. A double-clad design of the photonic lattice of the fiber is further postulated to enable a pump-related seeding mechanism of normal-dispersion supercontinuum broadening under sub-picosecond pumping, which is otherwise known for similar noise characteristics as modulation instability driven, soliton-based spectra.

World-smallest fiber-GRIN lens system for optofluidic applications

Filipkowski A.[1], Piechal B.[1], Pysz D.[1], Stepien R.[1], Cimek J.[1,2], Waddie A.[3], Klimczak M.[1], Stafiej P.[4], Taghizadeh M. R.[3], Buczynski R.[1,2,3]

[1] Department of Glass, Institute of Electronic Materials Technology, Wolczynska 133, 01-919 Warsaw, Poland

[2] Faculty of Physics, University of Warsaw, Pasteura 7, 02-093, Warsaw, Poland

[3] Department of Physics, School of Engineering and Physical Sciences, Heriot-Watt University, Scottish Universities Physics Alliance, Edinburgh, EH14 4AS, UK

[4] Faculty of Physics, Nicolaus Copernicus University, Grudziadzka 5, 87-10 Torun, Poland

Photonics Letters of Poland, 2016, 8, 2, 36 - 38

We have developed a new type of optical fiber probe which integrates a standard single mode fiber with a gradient index (GRIN) microlens. The system is perfectly suited for optofluidic sensor applications since the diameter of the lens module is exactly the same as that of the optical fiber. Moreover, the performance of the GRIN lens is not degraded by low contrast of the refractive index between the lens and the fluidic environment. The GRIN lens is made with a novel technology of nanostructured optics.

In situ Raman spectroscopy of the graphene/water interface of a solution-gated field-effect transistor: electron-phonon coupling and spectroelectrochemistry

Binder J.[1], Urban J. M.[1,3], Stepniewski R.[1], Strupinski W.[2], Wysmolek A.[1]

[1] Faculty of Physics, University of Warsaw, Pasteura 5, 02-093 Warsaw, Poland

[2] Institute of Electronic Materials Technology, Wólczyńska 133, 01-919 Warsaw, Poland

Nanotechnology, 2016, 27, 4

We present a novel measurement approach which combines the electrical characterization of solution-gated field-effect transistors based on epitaxial bilayer graphene on 4H-SiC (0001) with simultaneous Raman spectroscopy. By changing the gate voltage, we observed Raman signatures related to the resonant electron-phonon coupling. An analysis of these Raman bands enabled the extraction of the geometrical capacitance of the system and an accurate calculation of the Fermi levels for bilayer graphene. An intentional application of higher gate voltages allowed us to trigger electrochemical reactions, which we followed in. situ by Raman spectroscopy. The reactions showed a partially reversible character, as indicated by an emergence/disappearance of peaks assigned to C-H and Si-H vibration modes as well as an increase/decrease of the defect-related Raman D band intensity. Our setup provides a highly interesting platform for future spectroelectrochemical research on electrically-induced sorption processes of graphene on the micrometer scale.

Graphene growth on Ge(100)/Si(100) substrates by CVD method

Pasternak I.[1], Wesolowski M.[1], Jozwik I.[1], Lukosius M.[2], Lupina G.[2], Dabrowski P.[3], Baranowski J. M.[1], Strupinski W.[1]

[1] Institute of Electronic Materials Technology, Wolczynska 133, 01-919 Warsaw, Poland

[2] IHP, Im Technologiepark 25,15236 Frankfurt (Oder), Germany

[3] Department of Solid States Physics, University of Lodz, Pomorska 149/153, Lodz, 90-236, Poland

Scientific Reports, 2016, 6, 21773

The successful integration of graphene into microelectronic devices is strongly dependent on the availability of direct deposition processes, which can provide uniform, large area and high quality graphene on nonmetallic substrates. As of today the dominant technology is based on Si and obtaining graphene with Si is treated as the most advantageous solution. However, the formation of carbide during the growth process makes manufacturing graphene on Si wafers extremely challenging. To overcome these difficulties and reach the set goals, we proposed growth of high quality graphene layers by the CVD method on Ge(100)/Si(100) wafers. In addition, a stochastic model was applied in order to describe the graphene growth process on the Ge(100)/Si(100) substrate and to determine the direction of further processes. As a result, high quality graphene was grown, which was proved by Raman

spectroscopy results, showing uniform monolayer films with FWHM of the 2D band of 32 cm^{-1}.

Decrease of Nano-hardness at Ultra-low Indentation Depths in Copper Single Crystal

Kucharski S.[1], Jarząbek D.[1], Piątkowska A.[2], Woźniacka S.[1]

[1] Institute of Fundamental Technological Research, Warsaw, Poland

[2] Institute of Electronic Materials Technology, Warsaw, Poland

Experimental Mechanics, 2016, 56, 381 - 393

In the present study, we report a detailed investigation of the unusual size effect in single crystals. For the experiments we specified the hardness in single crystalline copper specimens with different orientations ((001), (011) and (111)) using Oliver-Pharr method. Our results indicates that with decreasing load, after the value of the hardness reached its maximum, it starts to decrease for very small indentation depths (<150 nm). For the sake of accuracy of hardness determination we have developed two AFM-based methods to evaluate contact area between tip and indented material. The proposed exact measurement of the contact area, which includes the effect of pile-up and sink-in patterns, can partially explain the strange behaviour, however, the decrease of hardness at low loads is still observed. At higher loads range the specified hardness is practically constant.

Microstructure and Thermoelectric Properties of Bulk Cobalt Antimonide ($CoSb_3$) Skutterudites Obtained by Pulse Plasma Sintering

Kruszewski M. J.[1], Zybała R.[1], Ciupiński Ł.[1], Chmielewski M.[2], Adamczyk-Cieślak B.[1], Michalski A.[1], Rajska M.[3], Kurzydłowski K. J.[1]

[1] Faculty of Materials Science and EngineeringWarsaw University of Technology, Warsaw Poland

[2] Institute of Electronic Materials Technology Warsaw Poland

[3] Faculty of Materials Science and Ceramics AGH University of Science and Technology, Krakow, Poland

Journal of Electronic Materials, 2016, 45, 3, 1369 - 1376

The use of the pulse plasma sintering technique for $CoSb_3$ thermoelectric material consolidation is reported in this work. The influence of sintering temperature on the microstructure and material properties such as the Seebeck coefficient, electrical resistivity, and thermal conductivity has been investigated. It is shown that, for samples fabricated at 923 K and 973 K, there were no significant differences in the average grain size or final phase composition. In both cases, a fine-grained polycrystalline structure of the compacts with density nearly equal to the theoretical value was achieved. Both samples were composed almost uniquely of $CoSb_3$ phase. The measured thermoelectric parameters such as the Seebeck coefficient, electrical, and thermal conductivity showed similar dependence on temperature. For both samples, the Seebeck coefficient was negative at room temperature and showed a transition from n- to p-type conduction over the temperature range of 400 K to 460 K. The measured minimum thermal conductivity values, 4 W m^{-1} K^{-1} to 5 W m^{-1} K^{-1} at 723 K, are typical for undoped bulk $CoSb_3$. A maximum ZT value of 0.08 at 623 K was obtained for the sample consolidated at 923 K for 5 min. The results of this work are very promising from the point of view of use of pulse plasma sintering as an alternative method for fabrication of a broad range of thermoelectric materials in the future.

Computationally-efficient FDTD modeling of supercontinuum generation in photonic crystal fibers

Karpisz T.[1], Salski B.[1], Buczynski R.[2,3], Kopyt P.[1], Pacewicz A.[1]

[1] Institute of Radioelectronics and Multimedia Technology Warsaw University of Technology, Warsaw, Poland

[2] Institute of Electronic Materials Technology, Warsaw, Poland

[3] Information Optics Group, Faculty of PhysicsWarsaw University, Warsaw, Poland

Optical and Quantum Electronics, 2016, 48, 175

It is shown in this paper that a finite-difference time-domain method can be successfully applied to rigorous electromagnetic analysis of supercontinuum generation in photonic crystal fibers. Large computational requirements of the method are alleviated by the use of a hybrid procedure where, at first, vector two-dimensional simulation is applied in order to determine mode properties of the fiber. Subsequently, one-dimensional simulation of a pulse propagating in a transmission line filled with effective material is performed. The parameters of the line take into account nonlinear characteristics of the filling material as well as the previously computed mode dispersion. It is depicted that the proposed novel hybrid approach opens the way for rigorous, yet, computationally-efficient modeling of third order nonlinear processes in optically long fibers. The example investigated in this paper shows very promising results as compared with experiments and approximate numerical simulations of a nonlinear Schrodinger equation performed with the aid of the split-step Fourier method.

Stable topological insulators achieved using high energy electron beams

Zhao L.[1], Konczykowski M.[2], Deng H.[1], Korzhovska I.[1], Begliarbekov M.[1], Chen Z.[1], Papalazarou E.[3], Marsi M.[3], Perfetti L.[2], Hruban A.[4], Wołoś A.[5,6], Krusin-Elbaum L.[1]

[1] Department of Physics, The City College of New York, CUNY, New York, New York 10031, USA.

[2] Laboratoire des Solides Irradie´s, E´cole Polytechnique, CNRS, CEA, Universite´ Paris-Saclay, 91128 Palaiseau cedex, France

[3] Laboratoire de Physique des Solides, CNRS, Universite´ Paris-Saclay, Universite´ Paris-Sud, 91405 Orsay, France.

[4] Institute of Electronic Materials Technology, 01-919 Warsaw, Poland.

[5] Institute of Physics, Polish Academy of Sciences, 02-668 Warsaw, Poland.

[6] Faculty of Physics, University of Warsaw, 00-681 Warsaw, Poland.

Nature Communications, 2016, 7, 10957

Topological insulators are potentially transformative quantum solids with metallic surface states which have Dirac band structure and are immune to disorder. Ubiquitous charged bulk defects, however, pull the Fermi energy into the bulk bands, denying access to surface charge transport. Here we demonstrate that irradiation with swift (~2.5 MeV energy) electron beams allows to compensate these defects, bring the Fermi level back into the bulk gap and reach the charge neutrality point (CNP). Controlling the beam fluence, we tune bulk conductivity from p- (hole-like) to n-type (electron-like), crossing the Dirac point and back, while preserving the Dirac energy dispersion. The CNP conductance has a two-dimensional character on the order of ten conductance quanta and reveals, both in Bi_2Te_3 and Bi_2Se_3, the presence of only two quantum channels corresponding to two topological surfaces. The intrinsic quantum transport of the topological states is accessible disregarding the bulk size.

Thulium Oxide Nanopowders Obtained by Precipitation

Sidorowicz A.[1,2], Wajler A.[1], Weglarz H.[1], Jach K.[1], Orlinski K.[1], Olszyna A.[2]

[1] Institute of Electronic Materials Technology, Wolczynska 133, Warsaw 01-919, Poland

[2] Warsaw University of Technology, Wołoska 141, Warsaw 02-507, Poland

Int. J. Appl. Ceram. Technol., 2016, 13, 2, 302 - 307

The aim of this work was to investigate the influence of precipitation parameters on the morphology of obtained thulium oxide powders. Tm_2O_3 precursor powders were synthesized by precipitation method using 0.1 - 0.25 M water solutions of thulium nitrate and 1.5 M ammonium hydrogen carbonate water solution as a precipitation agent. The processes were conducted at different temperatures (25 - 50 degrees C). The result showed that the morphology of the obtained thulium oxide (Tm_2O_3) powders depends both on the molar concentration of thulium nitrate and the temperature of precipitation. Small, round, loosely agglomerated Tm_2O_3 nanoparticles were obtained after air calcination of precursor precipitated at room temperature with the use of 0.1 M thulium nitrate solution.

Metal-ceramic functionally graded materials - manufacturing, characterization, application

Chmielewski M.[1], Pietrzak K.[1]

[1] Institute of Electronic Materials Technology, Wolczynska 133, Warsaw 01-919, Poland

Bulletin of the Polish Academy of Sciences Technical Sciences, 2016, 64, 1, 151 - 160

Functionally graded materials (FGMs) belong to a new, continuously developing group of materials, finding application in various branches of industry. The idea of freely designing their construction profile, restricted only by the available manufacturing techniques, enables obtaining materials with composition and structure gradients having unprecedented properties. In this paper, selected results of works carried out by the authors and relating to the application of the developed metal-ceramic composites were presented in order to manufacture functionally graded materials for target purposes. Gradient structures with various construction profiles that can play different roles were produced on the basis on the following material pairs: Cr-Al_2O_3, NiAl-Al_2O_3 and Cu-AlN. Manufacturing conditions, microstructure characteristics and selected properties, crucial from the point of view of future applications, were presented.

Performance analysis of thermally bonded Er^{3+}, Yb^{3+}:glass/Co^{2+}:$MgAl_2O_4$ microchip lasers

Mlynczak J.[1], Belghachem N.[1], Kopczynski K.[1], Kisielewski J.[2], Stepien R.[2], Wychowaniec M.[3], Galas J.[3], Litwin D.[3], Czyzewski A.[3]

[1] Institute of Optoelectronics Military University of Technology, Warsaw, Poland

[2] Institute of Electronic Materials Technology, Warsaw, Poland

[3] Maksymilian Pluta Institute of Applied Optics, Warsaw, Poland

Optical and Quantum Electronics, 2016, 48, 247

The new glass as well as Co^{2+}:$MgAl_2O_4$ saturable absorber synthesis, especially developed for thermal bonding, was described. The procedure of thermal bonding was presented. Generation parameters of continuous wave operation at 1.5 mu m wavelength were shown. The threshold below 180 mW and slop efficiency over 10 % was reached. Pulse generation in thermally bonded and unbonded as well as monolithic Er^{3+}, Yb^{3+}:glass/Co^{2+}:$MgAl_2O_4$ microchip lasers was compered. The peak power above 10 kW with pulse energy above 32 mu J and pulse width 3.2 ns was achieved.